# Importance of soil thermal regime in terrestrial ecosystem carbon dynamics in the circumpolar north

Yueyang Jiang[1, 5], Qianlai Zhuang[2*], Stephen Sitch[3], Jonathan A O'Donnell[4], David Kicklighter[5], Andrei Sokolov[6], and Jerry Melillo[5]

[1]Department of Earth, Atmospheric, and Planetary Sciences, Purdue University, West Lafayette, IN, USA

TEL: 1-508-289-7688 FAX: 1-508-457-1548 EMAIL: yjiang@mbl.edu

[2]Department of Earth, Atmospheric and Planetary Sciences and Department of Agronomy, Purdue University, West Lafayette, IN, USA

[3]Geography, College of Life and Environmental Sciences, University of Exeter, Exeter, UK

[4]Arctic Network, National Park Service, Fairbanks, AK, USA

[5]The Ecosystems Center, Marine Biological Laboratory at Woods Hole, MA, USA

[6]Dept. of Earth, Atmospheric, and Planetary Sciences, Massachusetts Institute of Technology, Cambridge, MA, USA

*Correspondence to: qzhuang@purdue.edu

**Keywords**: soil thermal regime, permafrost degradation, active layer, climate warming, carbon budget

## Abstract

In the circumpolar north (45-90$^{o}$N), permafrost plays an important role in vegetation and carbon (C) dynamics. Permafrost thawing has been accelerated by the warming climate and exerts a positive feedback to climate through increasing soil C release to the atmosphere. To evaluate the influence of permafrost on C dynamics, changes in

soil temperature profiles should be considered in global C models. This study incorporates a sophisticated soil thermal model (STM) into a dynamic global vegetation model (LPJ-DGVM) to improve simulations of changes in soil temperature profiles from the ground surface to 3 m depth, and its impacts on C pools and fluxes during the 20$^{th}$ and 21$^{st}$ centuries. With cooler simulated soil temperatures during the summer, LPJ-STM estimates ~0.4 Pg C yr$^{-1}$ lower present-day heterotrophic respiration but ~0.5 Pg C yr$^{-1}$ higher net primary production than the original LPJ model resulting in an additional 0.8 to 1.0 Pg C yr$^{-1}$ being sequestered in circumpolar ecosystems. Under a suite of projected warming scenarios, we show that the increasing active layer thickness results in the mobilization of permafrost C, which contributes to a more rapid increase in heterotrophic respiration in LPJ-STM compared to the stand-alone LPJ model. Except under the extreme warming conditions, increases in plant production due to warming and rising $CO_2$, overwhelm the enhanced ecosystem respiration so that both boreal forest and arctic tundra ecosystems remain a net C sink over the 21$^{st}$ century. This study highlights the importance of considering changes in the soil thermal regime when quantifying the C budget in the circumpolar north.

## 1. Introduction

Permafrost is an important control on vegetation and soil carbon (C) dynamics by affecting hydrological and soil thermal conditions in northern high-latitude ecosystems (Wania et al., 2009a; Schaphoff et al., 2013), which account for a large

49 portion of the global C stocks (Hugelius et al., 2014). Recent climate warming has
50 caused significant thawing of the near-surface permafrost across the circumpolar
51 region (Romanovsky et al., 2015), including Alaska (Jorgenson et al., 2006;
52 Osterkamp, 2007), Canada (Camill, 2005), and Russia (Streletskiy et al., 2015).
53 Projected warming over the 21$^{st}$ century is expected to greatly reduce the areal extent
54 of permafrost and seasonally frozen ground (Lawrence et al., 2012). If permafrost
55 thaws, a fraction of soil organic C (SOC) in previously frozen layers will decompose
56 and be released as $CO_2$ and $CH_4$ (Hayes et al., 2014; Walter-Anthony et al., 2014;
57 Olefeldt et al., 2012; Johnston et al., 2014). Furthermore, organic matter
58 decomposition rates in unfrozen soils are sensitive to soil temperatures, which vary
59 non-linearly across the soil column. Therefore, careful consideration of soil thermal
60 regime changes (i.e. soil temperatures across the soil column from surface to deep soil
61 layers) are important when simulating the potential future C loss from soils.
62 In addition to soil C pools, vegetation C pools are also sensitive to changes in soil
63 thermal dynamics by permafrost thaw and rates of associated biogeochemical
64 processes (Euskirchen et al., 2006). Field studies have indicated that permafrost thaw
65 increases aboveground net primary production via increased nutrient availability (e.g.,
66 Schuur et al., 2007). While not explicitly testing the effects of thaw, other model
67 studies have indicated a net C gain in circumpolar ecosystems because increased
68 vegetation productivity more than compensated belowground C losses under a
69 warming climate (Hartley et al., 2012; Koven, 2013). However, this net C gain may
70 be optimistic as the effects of water stress and disturbances (e.g. insect infestations,

71 wildfires) on permafrost-region biomass are not adequately incorporated in current
72 models (Abbott et al., 2016). Thus, large uncertainties currently exist regarding the
73 magnitude and timing of this permafrost-C feedback to the climate system (Schuur et
74 al., 2013), due in part to the complexity of ecosystem C processes in areas of
75 degrading permafrost (e.g., thermokarst, thermal erosion) and their heterogeneity
76 across regions.

77 To date, a number of studies have used process-based land surface models to
78 estimate permafrost-C feedbacks under projected thaw scenarios (Koven et al., 2011;
79 Schaefer et al., 2011; Harden et al., 2012; MacDougall et al., 2012; Schneider von
80 Deimling et al., 2012). Soil thermal dynamics within these models vary in their
81 complexity, from calculations of the cumulative active layer thickness distribution
82 (e.g., Harden et al., 2012) to more sophisticated parameterizations of soil physics (e.g.,
83 MacDougall et al., 2012). Thaw dynamics are typically considered in a top-down
84 one-dimensional manner, and heat transfer via conduction is the primary mode
85 considered. However, the importance of soil water in non-conductive heat transfer
86 (e.g., latent heat exchange, convection) has long been recognized as an important
87 control on soil thermal dynamics (e.g., Romanovsky and Osterkamp, 2000). In this
88 regard, our recent modeling studies that incorporate interactions between heat and
89 water transport (Jiang et al., 2012a) have shown improvements in simulating the soil
90 thermal regime changes in both tundra and boreal forest ecosystems in the northern
91 high latitudes (Jiang et al., 2015).

92 To provide a better quantification of the ecosystem C budget in northern high

93 latitudes and how this budget may change in the future, we use the
94 Lund-Potsdam-Jena Dynamic Global Vegetation Model (LPJ-DGVM, Sitch et al.,
95 2003; Gerten et al., 2004) coupled with a sophisticated soil thermal model (STM) by
96 Jiang et al. (2012a) to conduct a set of simulations for both historical and future
97 periods. The standard version of LPJ-DGVM has been widely used to simulate the
98 global C budget and its response to climate change (e.g., Sitch et al., 2008). However,
99 the model has used simplified soil temperature parameterizations for high-latitude
100 regions (Sitch et al., 2003). Although later studies by Wania et al. (2009a, b) have
101 taken steps to improve soil thermal and hydrologic parameterizations for permafrost
102 conditions in northern peatlands, soil temperature and water dynamics are still
103 modeled separately. As a consequence, the modeled active layer thickness exhibits
104 poor agreement with observations (Wania et al., 2009b). Moreover, the effects of the
105 vertical soil C distribution on decomposition have not been considered. In an
106 extended LPJ, which includes managed land (LPJmL), Schaphoff et al. (2013) have
107 recently coupled the interactions of soil water and heat transport, and considered
108 vertically differentiated soil C stocks based on an organized soil C dataset in Jobbagy
109 and Jackson (2000). However, the discrete vertical differentiation of the soil
110 temperature profile in LPJmL is relatively coarse and the vertical distribution of SOC
111 down to 3 m is highly concentrated in the uppermost soil layers (e.g., 0-20 cm) and
112 does not consider long-term SOC accumulation in deep soil layers (Hugelius et al.,
113 2014).

114 In this study, we integrate STM into LPJ to improve simulations of soil

115 temperature dynamics from the ground surface to a depth of three meters, and the
116 consequent impact on soil organic C stabilization and release across the northern
117 permafrost region. Because the newly coupled version of the model, LPJ-STM,
118 considers a fine vertical differentiation of soil temperatures, interactions of soil water
119 with heat transport, and a vertical distribution of SOC with more C in deeper soil
120 layers, we expect LPJ-STM to provide a more accurate quantification of the C budget
121 for historical periods and to improve projections of carbon dynamics under future
122 scenarios. To examine if LPJ-STM improved estimates of soil temperatures and
123 associated carbon dynamics over LPJ, we compare estimates of both models to site
124 observations of soil temperatures and net ecosystem production (NEP). In addition,
125 simulated atmospheric carbon dioxide concentrations determined by using the model
126 NEP estimates with an atmospheric transport model are compared to atmospheric
127 flask measurements. To examine how improvements in simulated soil thermal regime
128 affect the estimates of the contemporary C budget of northern high latitude
129 ecosystems and its projection into the 21$^{st}$ century, we compare estimates of net
130 primary production (NPP), heterotrophic respiration ($R_H$), and net ecosystem
131 production (NEP) as well as vegetation and soil C stocks between LPJ and LPJ-STM.
132

133 # 2. Methods

134 ## 2.1. Model description

135 LPJ model simulates large-scale vegetation structure and land-atmosphere C and
136 water fluxes in a modular framework (Sitch et al., 2003; Gerten et al., 2004). In the

standard LPJ soil model, two soil layers have a fixed depth (i.e. 0.5 m and 1.0 m). The vertical distribution of soil C within these two soil layers is not explicitly considered. For permafrost thermal dynamics, LPJ calculates soil temperature at a depth of 25 cm in a very simplistic way based on the surface air temperature seasonal cycle with a dampened oscillation about a common mean and with a temporal lag (Sitch et al., 2003). The magnitude of the damping and temporal lag is related to soil texture, and the applied function assumes a sinusoidal variation in seasonal temperatures (Campbell and Norman, 1998). In this study, we replace the existing soil temperature scheme in the original LPJ with STM (Jiang et al., 2012a) to produce the coupled LPJ-STM model. Meanwhile, we modified the hydrology scheme following Wania et al. (2009b) and the representation of soil carbon dynamics following Schaphoff et al. (2013) in the LPJ-STM model.

2.1.1. Soil thermal dynamics in LPJ-STM

While the original LPJ only includes a temperature calculation at a depth of 25 cm, LPJ-STM has a vertical differentiation of soil temperature profile and provides a more complete depiction of soil thermal dynamics, including estimates of active layer thickness (ALT). Here, we estimate ALT using the $0^{o}$C isotherm line as in Wania et al. (2009b). In LPJ-STM, the top three meters of soil is split into six layers with thicknesses of 10, 10, 10, 20, 50, and 200 cm (Figure 1) that differ with respect to physical and hydraulic properties of boreal forest and tundra sites (Jiang et al., 2012a). These soil layer thicknesses are finer than the five soil layers used by Schaphoff et al.

(2013) for the top 3 meters: 20, 30, 50, 100, and 100 cm. In addition, unlike Schaphoff et al. (2013), LPJ-STM divides each of the soil layers into a number of depth-step increments to calculate soil temperatures. From the first to the sixth layer, the number of depth-step increments is respectively 10, 10, 10, 10, 20, and 40. To simulate perennially frozen ground, soil between 3 and 50 m is classified as the seventh layer with soil temperature simulated at 0.5 m depth-step increments.

Soil temperature is simulated numerically at each depth step by solving a modified Richards equation (Hansson et al., 2004; Saito et al., 2006). The governing equation for heat transport is as follows:

$$\frac{\partial C_p T}{\partial t} - L_f \rho_i \frac{\partial \theta_i}{\partial t} + L_0(T)\frac{\partial \theta_v(T)}{\partial t} = \frac{\partial}{\partial z}\left[\lambda \frac{\partial T}{\partial z}\right] - C_w \frac{\partial q_l T}{\partial z} - C_v \frac{\partial q_v T}{\partial z} - L_0(T)\frac{\partial q_v}{\partial z} - C_w S T \quad (1)$$

where $C_p$ (J m$^{-3}$ K$^{-1}$) is the volumetric heat capacity of the soil, $C_w$ is the volumetric heat capacity of liquid water (4.18 × 10$^6$ J m$^{-3}$ K$^{-1}$), $C_v$ is the volumetric heat capacity of water vapor (1.2 × 10$^3$ J m$^{-3}$ K$^{-1}$), $\theta_i$ is the volumetric ice content (%), $\theta_v$ is the volumetric unfrozen water content (%), *t* is time (units), *z* is depth (m), *T* is the absolute temperature (K), $\rho_i$ is the density of ice (931 kg m$^{-3}$), $L_0$ is the volumetric latent heat of vaporization of liquid water (J m$^{-3}$), $L_f$ is the latent heat of freezing (3.34 $\times$10$^5$ J kg$^{-1}$), $\lambda$ is the apparent thermal conductivity of soil (J m$^{-1}$ s$^{-1}$ K$^{-1}$), $q_L$ is the flux density of liquid water, $q_v$ is the flux density of water vapor (m s$^{-1}$), and S is a sink term accounting for root water uptake (s$^{-1}$). While soil temperatures vary with depth step, the $\theta_i$ and $\theta_v$ used by LPJ-STM to calculate these temperatures (see below) are assumed to be uniformly distributed in each soil

180 layer (i.e., do not vary with depth steps within a soil layer).

181

182 2.1.2. Hydrology in LPJ-STM

183 To match the layering scheme in STM, we simply modify the hydrology in LPJ
184 partly following the routine in Wania et al. (2009b). The original top 0.5 m layer in
185 LPJ now corresponds to the top four layers in LPJ-STM and the bottom layer (from
186 0.5 m to 1.5 m) in LPJ is extended to 3 m depth and corresponds to the fifth and sixth
187 layer in LPJ-STM. The actual water holding capacity (*AWHC*, mm/mm) in each layer
188 *i* is determined as the difference between the water hold capacity (*WHC*, mm/mm)
189 and the ice content (*icefr*, mm/mm, estimated in STM):

190 $$AWHC_{(i)} = WHC_{(i)} - icefr_{(i)}$$

191 Of the top four layers (or top 50 cm, Figure 1), the change in water content (mm)
192 in each layer is determined as a layer-weighted difference of liquid water input (i.e.
193 rainfall and melting water) and output (i.e. soil evaporation and transpiration),
194 estimated in the LPJ hydrology module. In the top four layers, water in the *i*th layer
195 exceeding $AWHC_{(i)}$ is available for percolation into the $5^{th}$ and $6^{th}$ layers (Figure 1).
196 All these water fluxes (i.e., rainfall, melt water, soil evaporation, transpiration and
197 percolation) are estimated from the LPJ hydrology module (Gerten et al., 2004). In the
198 $5^{th}$ and $6^{th}$ layer, the change in water content is calculated as the difference between
199 percolation and transpiration. Within the $7^{th}$ layer, the soil water content is assumed to
200 be constant. The soil water content is updated daily in the hydrology routine, and then
201 passed on to STM to calculate the soil temperature of each depth step in each layer. In

the model, LPJ-STM does not consider hydraulic conductivity of water contents above field capacity. Roots can access water in all six layers as long as the layer is not frozen.

2.1.3. Soil carbon dynamics in LPJ-STM

To provide a vertical distribution of the C pool across the soil column to 3 m deep (six layers, Figure 1), we used a similar routine as that in Schaphoff et al. (2013):

$$SoilC_{(i)} = d_{(i)}^{K} SoilC_{total}$$

where $d$ (unitless) is the relative share of the $i$th layer in the entire soil pool and $K$ (unitless) is the slope parameter that characterizes the relative rate of decrease with depth. In Schaphoff et al. (2013), $K$ is varied by different plant functional types (PFTs) based on an optimized cumulative log-log equation from Jobbagy and Jackson (2000). Here, we use a $K$ value of 0.7 for all PFTs to estimate SOC stock in each layer, based on the information of vertical soil C distribution in the recent databases (FAO/IIASA/ISRIC/ISSCAS/JRC, 2012; Hugelius et al., 2014).

Change in the total soil C stock, $SoilC_{total}$ (g C/m$^2$), is determined by the C input to soil from litter (i.e. 30% of decomposed litter goes into the soil C pool) and the C loss from soil by decomposition ($k_{mean}$). The value of $k_{mean}$ is determined as a layer weighted sum of the mean decomposition rate $k_{mean_{(i)}}$ in each soil C layer:

$$k_{mean} = \sum_{i=1}^{nlayer} (k_{mean_{(i)}} \cdot d_{(i)}^{K})$$

Within each soil layer, we calculate the decomposition rate of each depth step using the same soil temperature and moisture-dependent scheme as in Sitch et al. (2013).

Then we determine $k_{mean_{(i)}}$ as the mean decomposition rate of all depth steps within the *i*th layer:

$$k_{mean_{(i)}} = \frac{1}{n_{depthsteps}} \sum_{j=1}^{n_{depthsteps}} k_j$$

For example, $k_{mean_{(i)}}$ of the 1st layer is the mean of decomposition rates of all 10 depth steps (each step is 1 cm thick). This is different from Schaphoff et al. (2013), in which $k_{mean_{(i)}}$ is calculated using the mean soil temperature and soil moisture of layer *i*.

To mechanistically simulate the C shift between layers, following Schaphoff et al. (2013), the annual shift of C input $C_{shift_{(i)}}$ (unitless) for soil layer *i* into the lower layer due to cryoturbation and bioturbation is estimated by:

$$C_{shift_{(i)}} = \frac{d_{(i)}^{K} k_{mean_{(i)}}}{k_{mean}}$$

## 2.2. Climate forcing

In this study, monthly air temperature, cloud cover, precipitation, number of wet days, atmospheric $CO_2$ concentrations and soil property data are used to drive both LPJ and LPJ-STM. Historical climate data for 1901-2000 are obtained from the Climate Research Unit (CRU; Mitchell and Jones, 2005). The historical atmospheric $CO_2$ concentration datasets are from ice-core records and atmospheric observations (Keeling and Whorf, 2005), and soil texture data is derived from the FAO soil datasets (Zobler, 1986; FAO, 1991).

For the period 2001-2100, we use six climate scenarios produced with the MIT

245 Integrated Global System Model (IGSM; Sokolov et al., 2005) under two emission
246 scenarios (reference and level 1 stabilization cases, Table 1) in the Synthesis and
247 Assessment Product 2.1 of the U.S. Climate Change Science Program (Clarke et al.,
248 2007; Webster et al., 2012). The reference emission scenario (REF), which assumes
249 no climate policy, is very similar to the IPCC RCP8.5 scenario. The average $CO_2$
250 concentration over last decade of the 21$^{st}$ century in the IGSM REF simulations, with
251 median settings for C cycle parameters and reference emission scenario, is 870 ppm
252 (Sokolov et al., 2009; Webster et al., 2012), compared to 890 ppm from the IPCC
253 RCP8.5 scenario. The corresponding total greenhouse gas forcing is an equivalent
254 $CO_2$ concentration of 1330 and 1250 ppm, respectively. In contrast, the level 1
255 stabilization scenario (POL) assumes a rather stringent climate policy with global
256 greenhouse gas emissions declining from year 2015 to year 2060 and staying fixed
257 thereafter. As a result, $CO_2$ concentrations increase by the end of 21$^{st}$ century to only
258 480 ppm (560 ppm of $CO_2$-equivalent), which falls in between the values for the
259 IPCC RCP4.5 and RCP2.6. More detailed comparisons between the RCPs and the
260 scenarios used in this study can be found in Webster et al. (2012).

261 Climate simulations for the two emission scenarios are carried out using three
262 different sets of parameters defining the climate system responses to anthropogenic
263 emissions. These responses are dependent on climate sensitivity, the rate of heat
264 uptake by the deep ocean, and the strength of aerosol forcing for a given emissions
265 loading. Climate parameter sets corresponding to the 5$^{th}$, 50$^{th}$ and 95$^{th}$ percentiles of
266 the probability distribution for the increase in surface air temperature in the last

decade of 21st century in the ensembles of simulations with REF and POL emissions (Sokolov et al., 2009) are chosen to represent low (L), median (M) and high (H) climate responses, respectively. The 90% probability ranges for the 21st century surface warming relative to 1981-2000 are 3.7-7.4$^{o}$C and 1.1-2.5$^{o}$C for the REF and POL scenarios respectively, with median values of 5.1$^{o}$C and 1.6$^{o}$C (Sokolov et al., 2009; Webster et al., 2012). Thus results from six simulations used in this study (REF_M, REF_L, REF_H and POL_M, POL_L, POL_H) cover a very wide range of possible changes in future climate.

### 2.3. Simulation Protocols

Both the LPJ and LPJ-STM simulations are initially run for 2000 "spin-up" years before 1901, using a cyclic replication of climate data from 1901 to 1930. Similar to the strategy in Schaphoff et al. (2013), the first 990 years spin-up for LPJ-STM is run to achieve an equilibrium state of vegetation cover and mean-annual litter input into soils. The size of the slow soil C pool is analytically solved assuming a mean climate condition, and then we run for a further 1010 years with climate variability to initialize the soil C pool for each soil layer. From 1901 to 2100, the historical data (CRU, 1901-2000), followed by each of the six projected IGSM climates and $CO_2$ concentrations, are used to drive the simulations for the study region, which is represented by a total of 25,063 grid cells at a 0.5$^{o}$ latitude × 0.5$^{o}$ longitude resolution.

### 2.4. Evaluation of model performance

We compare the LPJ and LPJ-STM modeled soil temperatures with observations from eight sites studied in Jiang et al. (2012a). To evaluate the model performance for simulating C dynamics, we first compare the simulated C fluxes from both LPJ and LPJ-STM to the measured NEP from FLUXNET sites (http://fluxnet.ornl.gov). We also examine the ability of each model to reproduce seasonal fluctuations in atmospheric $CO_2$ concentration by using the modeled NEP across the circumpolar region to drive an atmospheric inversion and transport model TM2 (Kaminski et al., 1999). The simulated $CO_2$ concentrations are then compared with the atmospheric flask measurements from monitoring stations. As in Heimann et al. (1998), we calculate the normalized mean-squared deviation (NMSD, equation is shown in Table 2) to evaluate the goodness of fit between the simulated and observed seasonal atmospheric $CO_2$ concentration.

# 3. Results

## 3.1. Model performance

The LPJ-STM is able to well simulate the soil temperature profile for high latitude sites (Figure 2). When compared with measured soil water content at 25 cm, LPJ-STM shows clearly better agreement than LPJ (Figure 3). The LPJ-STM soil temperature estimates have lower root mean square error (RMSE) values than the LPJ estimates when compared against field measurements (Figure 4). By replacing the LPJ soil temperature model with the STM, the seasonal temperature fluctuations are dampened with a much cooler soil during the growing season (the duration of the

311 annual non-frozen period of the top 25 cm of soil) and a slightly warmer soil during
312 the cold period (September - May). As shown in Jiang et al. (2012a), the soil
313 temperature profile simulated by STM shows good agreement with observations at 11
314 sites, but the discrepancy between modeled and measured soil temperatures tends to
315 increase with profile depth. Our model shows a clear latitudinal gradient of ALT in the
316 circumpolar north (Figure 5). Compared with ALT observations from 172 sites in
317 GTN-P database (Biskaborn et al., 2015), a simple linear regression indicates a good
318 agreement in general trends between modeled historical ALT and site observations
319 (Figure 5). However, the model tends to overestimate ALT at sites where the observed
320 ALT is less than 100 cm and underestimate ALT at sites where the observed ALT is
321 greater than 100 cm.

322 Compared with measured NEP at FLUXNET sites, LPJ-STM performs better than
323 LPJ in reproducing monthly NEP (Figure 6), based on more accurate simulation of
324 NEP during the growing season. The larger amplitudes of the seasonal NEP cycles
325 produced by LPJ-STM are mainly due to the lower summer $R_H$ and higher winter $R_H$,
326 relative to LPJ estimates. When we use the NEP estimates from LPJ and LPJ-STM
327 separately as inputs for TM2, and we find that the NEP from LPJ-STM leads to a
328 larger amplitudes of the seasonal cycles of $CO_2$. This seasonal pattern is more
329 comparable with observations from not only the northern stations, but also stations in
330 the tropics ($30^oN – 30^oS$, e.g., Ascension Island) and Southern Hemisphere ($30^oS$
331 southward; e.g., Cape Grim, Tasmania), where the seasonal cycle is still largely
332 influenced by atmospheric transport of $CO_2$ from the northern biosphere. Compared

333 with NMSD values for models in Heimann et al. (1998), LPJ-STM performs better in
334 reproducing the seasonal cycle of atmospheric $CO_2$ (Table 2).
335
336 **3.2. Changes in permafrost extent**
337 The LPJ-STM projections indicate potential large changes in future soil thermal
338 dynamics of circumpolar ecosystems. The model results show a substantial decrease
339 in the extent of near-surface permafrost under the projected IGSM climates with the
340 changes in extent being largely dependent on the warming strength (Figure 7).
341 Throughout the 21$^{st}$ century, the modeled decrease in permafrost extent varies among
342 different climate scenarios, and the rate of permafrost loss increases during the second
343 half of the century. In particular, under the REF_H scenario, nearly 88% of
344 near-surface permafrost (i.e. in top 3 meters) will disappear by 2100, when there will
345 be only relict permafrost at depths untied to prevailing climatic conditions (Figure 7).
346 Under the POL_L scenario, only about 15% near-surface permafrost will disappear
347 throughout the same time period. In general, the REF emission scenarios correspond
348 to a larger loss of permafrost than the POL emission scenarios.
349
350 **3.3. Carbon budget**
351 **3.3.1. Present-day**
352 The two models achieve different initial equilibrium states in the year 1901, in
353 which LPJ-STM estimates a smaller area covered by boreal deciduous forests than
354 LPJ because LPJ-STM projects a shorter growing season and the photosynthesis of

355 boreal deciduous trees is concentrated during the growing season. Instead, LPJ-STM
356 estimates a larger area covered by evergreen forests than LPJ because the
357 mid-summer NPP of boreal needleleaved trees is highly influenced by summer root
358 respiration, which is lower in LPJ-STM because of the lower summer soil
359 temperatures than that estimated with LPJ. Consequently, LPJ-STM estimates larger
360 vegetation and soil C stocks (+13.7 Pg C or +8% and +430.2 Pg C or +50%,
361 respectively, Table 3), and approximately 1.1 Pg C $yr^{-1}$ higher NEP than LPJ during
362 the 1900s (Figure 8).

363 Throughout the $20^{th}$ century, LPJ-STM consistently yields ~0.5 Pg C $yr^{-1}$ higher
364 NPP than LPJ, despite the shorter growing season. Compared with LPJ, the growing
365 season length as simulated by LPJ-STM is 14±8 days shorter at present, primarily due
366 to later spring thaw (~10±6 days), and to a lesser extent due to earlier refreezing in
367 autumn (~4±3 days). Unlike NPP, the difference in annual $R_H$ between LPJ-STM and
368 LPJ gradually decreases from -0.6 Pg C $yr^{-1}$ in 1900s to around -0.4 Pg C $yr^{-1}$ for
369 2000s (Figure 8). Larger NPP and smaller $R_H$ in LPJ-STM translates to 0.8 - 1.0 Pg C
370 $yr^{-1}$ higher NEP in the 2010s, relative to those in LPJ. Spatially, almost the whole area
371 underlain by permafrost (Figure 5) exhibits stronger C sequestration in LPJ-STM
372 relative to LPJ (Figure 9). In particular, the strongest enhancement in annual NEP
373 (+50 to +100 g C $m^{-2}$ $yr^{-1}$) occurs in the Canadian boreal forest, Eastern Siberia and
374 Mongolia, while the greatest reduction occurs in western Russia with up to a 90 g C
375 $m^{-2}$ $yr^{-1}$ decrease in annual NEP.

376 The larger NPP in LPJ-STM maintains a higher vegetation C pool at present (i.e.

227.7 – 229.4 Pg), which is about 17.2 - 18.1 Pg C higher than in LPJ (i.e. 210.1 – 211.8 Pg, Table 3). Generally, the additional vegetation C estimated by LPJ-STM occurs mostly in boreal forest zones (e.g., the Alaskan and Canadian boreal forests) with up to 1.1 kg C $m^{-2}$ increases in vegetation C density (Figure 9). Higher NPP also leads to more litter C input into the soil, and together with the lower $R_H$ contributes an ~430 Pg larger soil C pool in LPJ-STM during the 2010s (i.e. ~1297 Pg C, Table 3). The major differences in simulated soil C pool between the two models occur in the boreal forest eco-regions (e.g., the Alaskan, Canadian and Siberian boreal forests), where LPJ-STM produces up to 20 kg C $m^{-2}$ higher soil C stocks (Figure 9). The LPJ-STM simulations indicate that the continuous permafrost in the far northern regions and Mongolia store the largest soil C pools in the circumpolar north.

LPJ-STM permafrost better than LPJ in simulation SOC pool, when compared with two major global soil C datasets. In particular, LPJ-STM estimates higher soil C than the land-based Harmonized World Soil Database (HWSD, FAO/IIASA/ISRIC/ISSCAS/JRC, 2012), but lower soil C in permafrost areas (~17.8 $\times 10^6$ $km^2$, Figure 10) defined by the Northern Circumpolar Soil Carbon Database version 2 (NCSCDv2, Tarnocai et al., 2009; Hugelius et al., 2014). In particular, LPJ-STM estimates 177 Pg C for the top 30 cm of the soil profile compared to 151 Pg C by HWSD and 217 ± 12 Pg C by NCSCDv2. For the top 100 cm of the soil profile, LPJ-STM estimates 389 Pg C compared to 288 Pg C by HWSD and 472 ± 27 Pg C by NCSCDv2. The higher SOC stocks estimated by LPJ-STM relative to HWSD occur in most areas underlain by permafrost (e.g., Siberia, Alaska, and Canadian boreal

399 forest and tundra, Figure 10). The lower SOC stocks estimated by LPJ-STM relative
400 to NCSCDv2 mainly occur in Siberia.
401
402 **3.3.2. Future carbon budgets**
403 Under the warming scenarios, both models predict significant increases in annual
404 NPP and $R_H$, where the magnitude is largely controlled by the level of climate change
405 (Table 4). In particular, the reference climate scenarios cause an approximate increase
406 of 47-59% in annual NPP by 2100, but only ~10% accrual under the policy climate
407 scenarios (Table 4). In parallel, the NPP difference between LPJ-STM and LPJ
408 increases from around 0.5 Pg C $yr^{-1}$ to 0.8-0.9 Pg C $yr^{-1}$ under the reference scenarios,
409 but exhibits only a slight increase (~0.1 Pg C $yr^{-1}$) under the policy scenarios (Figure
410 8). Changes in $R_H$ show similar patterns of response to the climate variability as those
411 of NPP (Table 4), while the difference in $R_H$ between the two models shows a clear
412 decreasing trend through all six warming scenarios (Figure 8).
413 As the difference of NPP and $R_H$, the NEP in both models is simulated to decrease
414 over the 21$^{st}$ century, because the annual $R_H$ increases faster than NPP, especially
415 under the severe warming scenarios (Table 4). For example, forced by the REF_M
416 and REF_H scenarios, the study region eventually shifts from a C sink to a source by
417 2090s. Meanwhile, the NEP difference between the two models exhibits a clear
418 decline (from ~0.9 to ~0.6 Pg C $yr^{-1}$) through the 21$^{st}$ century, despite the strong
419 inter-annual variability (Figure 8). However, the significant positive difference here
420 indicates that the introduction of STM into LPJ contributes to maintaining the

421 modeled capacity of C sequestration in the circumpolar north.

422 Given the enhanced plant productivity associated with warming and $CO_2$ increase,
423 both models predict a large increase in the vegetation C pool, which is 18.4 – 22.3 Pg
424 C larger in LPJ-STM (294.1 - 358.0 Pg C) than in LPJ (275.7 - 336.4 Pg C) by 2090s
425 (Table 3). Driven by six warming scenarios, LPJ projects substantive soil C loss
426 ( -26.5 to -58.8 Pg C), and LPJ-STM projects a 2.8 - 34.1 Pg C gain in soil C stock
427 over the period of 2000 – 2100 under four out of the six IGSM climates but 5.3 and
428 27.1 Pg soil C loss under REF_M and REF_H (Table 3).

429

430 ## 4. Discussion

431 In this study, we examine how a more detailed representation of soil thermal
432 dynamics, soil hydrology, and soil C dynamics influences estimates of C fluxes and
433 pools of ecosystems in the circumpolar north. The detailed representation of these
434 ecosystem processes in LPJ-STM estimates higher NPP, but lower RH for current
435 circumpolar ecosystems than the more aggregated representation of these processes in
436 LPJ. As a result, more C (0.8 to 1.0 Pg C $yr^{-1}$) is estimated to be sequestered in these
437 ecosystems by LPJ-STM with almost all of the additional C (96%) being stored in
438 soils. With global warming, the LPJ-STM still estimates more C is sequestered in the
439 future than LPJ with most of the additional C being stored in soils, but the difference
440 between model estimates decrease over time. Below we focus our discussion on: 1)
441 how the LPJ-STM improved the quantification of present-day C budgets; 2) how
442 these improvements affect projections of future permafrost degradation and their

443 effects on C dynamics; and 3) sources of uncertainty in simulating C dynamics in the
444 circumpolar north region.
445
446 **4.1. Present-day soil C budgets**
447 The increase in annual $R_H$ as simulated in both models is mainly driven by the
448 warming soil temperatures. The addition of vertical differentiation of the soil
449 temperature profile and a depth distribution of soil C in LPJ-STM improves the
450 representation of soil physical and biogeochemical processes. This leads to a more
451 accurate simulation of thawing and refreezing processes as well as ALT estimates,
452 further reducing the model errors in soil C stock. The lower summer soil temperatures
453 produced by LPJ-STM largely stabilize soil C by reducing $R_H$, especially for the top
454 layers (e.g., the upper 30 cm, Figure 10). The impact of considering permafrost on $R_H$
455 in our simulation is different from Wania et al. (2009a), who shows that the
456 introduction of permafrost increases soil respiration by about 0.39 Pg C $yr^{-1}$ probably
457 because LPH-WHy simulates higher soil C stock (+39 Pg C) over 1991-2000.
458 However, LPJ-STM estimates lower (-0.6 Pg C $yr^{-1}$) $R_H$ than LPJ mainly because
459 LPJ-STM estimates significantly lower summer soil temperatures than LPJ, even
460 though LPJ-STM has a larger soil C pool than LPJ. As demonstrated in Schaphoff et
461 al. (2013), saturated hydraulic conductivity may also play an important role in the C
462 balance, as $R_H$ achieves peak rates around field capacity and decreases as water
463 saturation is approached because of decreasing soil oxygen content. Because we did
464 not consider water contents above field capacity in our analyses, $R_H$ may be

somewhat overestimated in our study. In addition, $R_H$ may also be overestimated at sites where the model overestimates the size of the active layer (Figure 5). Consequently, our estimates of soil C pool in the circumpolar north may be conservative, especially in regions with high water content (e.g., wetland).

The slightly lower SOC from LPJ-STM relative to NCSCDv2 is probably due to not considering the effects of some important processes in our model that influence deep C storage in the northern permafrost region, such as peatland development (Smith et al., 2004; Treat et al., 2016), syngenetic permafrost aggradation in areas of loess deposition (i.e. Yedoma; Shur et al. 2004), and alluvial deposition (i.e. large river deltas; Hugelius et al., 2014). Northern peatlands in particular store large amounts of SOC, with approximately 184 and 94 Pg C in Histels (i.e. permafrost peatlands) and Histosols (non-permafrost peatlands), respectively (Tarnocai et al., 2009; Yu et al., 2010). Moreover, the model-data differences could be partly attributed to the spatial heterogeneity caused by disturbances that have not been explicitly simulated in the model, such as fire and thermokarst (Grosse et al., 2011). Similar to our results, lower estimates of SOC relative to NCSCDv2 have been observed in other earth system models (Todd-Brown et al., 2013). Compared with HWSD, LPJ-STM estimates higher SOC stocks in most of the permafrost affected areas. It is difficult to evaluate these differences, however, because HWSD has not included enough information about how their estimates were derived.

We estimate that approximately 844 Pg C are stored within the top 3 m of soils, which is slightly lower than the estimates of 1035 ± 150 Pg C in Hugelius et al.

(2014). We recognized that, in parts of the circumpolar north, soils might not extend to a depth of 3 meters or even be present in areas with bedrock near or at the surface. In other areas, there is widespread occurrence of massive ground ice (Schirrmeister et al., 2011) as in regions with deep yedoma deposits (Kanevskiy et al., 2011). Because these factors are not accounted for in LPJ-STM, our model may overestimate the SOC stocks in the region. Meanwhile, some important soil forming processes (e.g., peat formation, cryoturbation) that greatly influence the distribution of SOC in deep soil layers (Bockheim, 2007; Hugelius et al., 2010) are not mechanistically modeled, which may cause bias in SOC estimates, especially in the mineral soil layers. Therefore, in ice-rich permafrost areas, model-data differences in deep layer SOC can be substantial. However, due to the scarce field data (i.e. few sampled pedons) and limited quantification of spatial variability in both ground ice content and soils, the empirical SOC data in some remote areas (Mishra et al., 2013), and in regions of thin sedimentary overburden (e.g., highlands and alpine terrain) have relatively high uncertainty (Hugelius et al., 2014). Therefore, more field measurements in deep soil layers and representation of spatial distribution of shallow soils and ground ice are needed to better constrain the regional simulations of SOC in the permafrost zone.

LPJ-STM produces lower $R_H$ than LPJ mainly because of the lower summer soil temperatures in the active layer and the freezing conditions below, where microbial activity is limited. The higher NPP in LPJ-STM is a counter-balance between the reduced summer below-ground autotrophic respiration due to cooler soil temperature, and the decrease in water availability associated with the decreased rooting depth in

permafrost affected areas. The enhancement in $CO_2$ exchange through amplified plant productivity in LPJ-STM is consistent with the finding in Forkel et al. (2016). However, our simulation results are different from Wania et al. (2009a), who show that integrating a simple permafrost model into LPJ slightly reduced circumpolar (45-90$^{o}$N) NEP due to the decrease in NPP and increase in $R_H$.

### 4.2. Permafrost degradation and its implications for future carbon budget

Compared with the simulated permafrost extent in Lawrence et al. (2012), our study estimates a slightly larger extent of the entire permafrost zone in the early 2000s. Driven by the range of MIT IGSM climate scenarios, we estimate large variabilities in permafrost extent by 2100 (Figure 7), which are comparable to the projections in Slater and Lawrence (2013). The lower boundary of modeled permafrost retreat (i.e. ~23% reduction in permafrost area under the coolest climate, POL_L), is similar to the estimate in a conservative permafrost model (Anisimov and Reneva, 2006) that predicts an approximate 19-24% reduction in near-surface permafrost area by 2080. At the biome level, our simulated range of permafrost degradation also covered the estimates from other model simulations. For example, our projected permafrost extent under the IGSM policy scenarios in the Canadian boreal forest region is similar to Zhang et al. (2008) who show a 15 - 19% reduction in the extent of permafrost through the 21$^{st}$ century. Although the rate of permafrost retreat could potentially be faster than the migration of boreal deciduous forests, the presence of permafrost still constrains the northward expansion of boreal broadleaved summergreen trees, which

is consistent with the findings in Tchebakova et al. (2009). As the southern boundary of permafrost moves northward, temperate forests are projected to migrate to the north and gradually replace the boreal forests. This expansion is partly because temperate trees are favored in the warming climate in our model.

The reduced difference in future NEP between LPJ-STM and LPJ (Figure 8) occur for a number of reasons. The more positive effect of permafrost on the C sink by LPJ-STM compared to LPJ will decrease as the permafrost degrades because more of the newly thawed labile SOC pool will be exposed to decomposition in LPJ-STM. The projected replacement of boreal evergreen conifer forests with herbaceous and deciduous vegetation in the thawing permafrost area can influence the C inputs to mineral soil, because of variations in productivity among these biomes (Jobbagy and Jackson, 2000) and in the ability of roots to access the mineral substrate (O'Donnell et al., 2011). As permafrost thaws, areas with a transition from boreal evergreen forest to temperate deciduous forest exhibit a fast decline in annual NEP, although the NPP increases rapidly due to a larger temperature range for temperate types (Sitch et al., 2008). This implies that the enhancement in biomass productivity by vegetation change in boreal zone could not offset the C loss through increased $R_H$ by warming climate. Because both models predict a declining trend in annual NEP, the reduced model difference implies a faster reduction in NEP by LPJ-STM. This indicates a high sensitivity of C sequestration to permafrost degradation, especially under severe warming scenarios (e.g., REF_H).

Unlike LPJ that projects a reduced SOC pool throughout the 21$^{st}$ century because

553 of the warming-stimulated SOC decomposition, LPJ-STM predicts a gain in the SOC
554 pool over the current century. In LPJ-STM, increased litter C inputs from the
555 stimulated plant growth are sufficient to compensate for the loss of SOC by
556 decomposition, which is greatly suppressed by the simulated cooler summer soil
557 temperature (Table 3). However, we also notice that as soil temperature increases,
558 litter decomposition becomes stronger and the amount of decomposed litter turning
559 into SOC becomes insufficient to compensate for the respiratory C loss from soil. As
560 a result, SOC accumulation slows down and even declines during the second half
561 century under severe warming scenarios (e.g., REF_H, Table 3).
562
563 **4.3. Sources of uncertainty**
564 Despite the improved simulation of soil temperatures, LPJ-STM still likely
565 overestimates NPP because nitrogen limitations to NPP have not been explicitly
566 considered as in other modeling studies (Sokolov et al., 2008; Xu and Prentice, 2008;
567 Smith et al., 2014) or shown in field studies (Nordin et al., 2004; Hobara et al., 2006).
568 However, increased nitrogen mineralization associated with enhanced decomposition
569 from permafrost degradation (Keuper et al., 2012; Koch et al., 2013, 2014;
570 Walter-Anthony et al., 2014; Hayes et al., 2014) may cause nitrogen to be more
571 available to NPP in permafrost environments than in other biomes under warming
572 conditions, especially in well-drained tundra ecosystems with deep rooting zones
573 (Shaver et al., 2001; Mack et al., 2004; Schuur et al., 2007).
574 Permafrost degradation can also cause a substantial change in surface hydrology,

which will further influence the vegetation dynamics and C balance in the region. For example, in ice-rich and poorly-drained permafrost areas, permafrost degradation will cause substantial ground-surface subsidence and ponding where the over-saturated conditions may increase tree mortality in boreal forests (Osterkamp et al., 2000; Jorgenson et al., 2001). Long-term permafrost degradation will eventually promote subsurface water drainage and increase the dryness of soils (Yoshikawa and Hinzman, 2003). In peatlands, the warming-caused declines in water table may increase soil decomposition, leading to a long-term C loss (Ise et al., 2008; Oechel et al., 1998; Sulman et al., 2009; Olivas et al., 2010). In contrast, a low water table may cause a long-term C gain in non-peat wetlands (Sulman et al., 2010). Given the importance of hydrological change on C balance, future C models should be coupled with climate-driven hydrological models (e.g., Wania et al., 2009a,b).

Another uncertainty source is fire disturbance. Future stimulated fire regimes in both boreal forest (Turetsky et al., 2011), and tundra landscapes (Rocha et al., 2012) will exacerbate the permafrost degradation rate relative to the change from warming alone (Lawrence et al., 2012; Schuur et al., 2013; Jiang et al., 2015). Fires may therefore play a more important role in C dynamics of the circumpolar north. However, the fire-caused change in permafrost thaw has not been accounted in current modeling work. A more mechanistic description for the relationships between fire, permafrost and C dynamics is necessary for future modeling efforts.

## 5. Conclusions

This study examines the importance of the changes of soil thermal regime in determining the C budget in the circumpolar north. With explicitly modeled temperatures at different depths, the LPJ-STM model estimates larger soil organic C stocks in the circumpolar north, which agrees well with empirical global data source. Our model simulations indicate that, although most biogeochemical processes of C storage and decomposition take place in top soil layers (i.e. top 30 cm), deep layers also substantially influence the SOC dynamics, especially when these layers confront a phase change. Some missing processes that affect the soil thermal regimes (e.g., formation of taliks, absence of snow dynamics) result in a significant uncertainty of our estimates. Thus more field measurements of deep soil organic carbon are needed. This study highlights the importance of more adequate representation of soil thermal dynamics in dynamic global vegetation models, such as LPJ, for quantifying C responses to climate change in northern high latitudes.

## Acknowledgment

We thank Jessica Drysdale for comments on earlier drafts of this manuscript. This research is supported by funded projects to Q. Z. National Science Foundation (NSF--1028291 and NSF- 0919331), the NSF Carbon and Water in the Earth Program (NSF-0630319), the NASA Land Use and Land Cover Change program (NASA-NNX09AI26G), and Department of Energy (DE-FG02-08ER64599). The computing is supported by Rosen Center of high performance computing at Purdue.

# References


Abbott, B. W., et al., 2016. Biomass offsets little or none of permafrost carbon release from soils, streams, and wildfire: an expert assessment. Environmental Research Letters 11, 034014, doi: 10.1088/1748-9326/11/3/034014.

Anisimov, O.A., Reneva, S., 2006. Permafrost and changing climate: The Russian perspective. Ambio 35(4), 169–175.

Biskaborn, B.K., Lanckman, J.P., Lantuit, H., Elger, K., Dmitry, S., William, C., Vladimir, R., 2015. The new database of the Global Terrestrial Network for Permafrost (GTN-P). Earth System Science Data, 7, 245-259.

Bockheim, J.G., 2007. Importance of cryoturbation in redistributing organic carbon in permafrost-affected soils. Soil Sci. Soc. Am. J. 71, 1335–1342.

Camill, P., 2005. Permafrost thaw accelerates in boreal peatlands during late-20th century climate warming. Clim. Change 68, 135–152.

Campbell, J.S., Norman, J.M., 1998. An Introduction to Environmental Biophysics, 286 pp., Springer.

Clarke, L., Edmonds, J., Jacoby, H., Pitcher, H., Reilly, J., Richels R., 2007. Scenarios of Greenhouse Gas Emissions and Atmospheric Concentrations, Sub-report 2.1A of Synthesis and Assessment Product 2.1 by the U.S. Climate Change Science Program and the Subcommittee on Global Change Research. Department of Energy, Office of Biological and Environmental Research, Washington, DC., USA, 106 pp.

Euskirchen, S.E., McGuire, A.D., Kicklighter, D.W., Zhuang, Q., Clein, J.S., Dargaville. R.J., Dye. D.G., Kimball, J.S., McDonald, K.C., Melillo, J.M., Romanovsky, V.E., Smith, N.V., 2006.

641 Importance of recent shifts in soil thermal dynamics on growing season length, productivity,
642 and carbon sequestration in terrestrial high-latitude ecosystems. Global Change Biology 12,
643 731-750.
644 FAO, 1991. The digitized soil map of the world (Release 1.0). Food and Agriculture Organization
645 of the United Nations, 67(1), Rome.
646 FAO/IIASA/ISRIC/ISSCAS/JRC, 2012. Harmonized World Soil Database (version 1.2). FAO,
647 Rome, Italy and IIASA, Laxenburg, Austria.
648 Forkel, M., Carvalhais, N., Rödenbeck, C., Keeling, R., Heimann, M., Thonicke, K., Zaehle, S.,
649 Reichstein, M., 2016. Enhanced seasonal $CO_2$ exchange caused by amplified plant productivity
650 in northern ecosystems. Science 351(6274), 696-699.
651 Gerten, D., Schaphoff, S., Haberlandt, U., Lucht, W., Sitch, S., 2004. Terrestrial vegetation and
652 water balance – hydrological evaluation of a dynamic global vegetation model. Journal of
653 Hydrology 286, 249–270.
654 Grosse, G. et al., 2011. Vulnerability of high-latitude soil organic carbon in North America to
655 disturbance. J. Geophys. Res. 116, G00K06, doi:10.1029/2010JG001507.
656 Harms, T.K., Jones, J.B., 2012. Thaw depth determines reaction and transport of inorganic
657 nitrogen in valley bottom permafrost soils. Global Change Biology 18, 2958–2968.
658 Hansson, K., Šimůnek, J., Mizoguchi, M., Lundin, L., van Genuchten M.Th., 2004. Water flow
659 and heat transport in frozen soil: numerical solution and freeze–thaw applications. Vadose
660 Zone Journal 3, 693–704.
661 Harden, J.W. et al., 2012. Field information links permafrost carbon to physical vulnerabilities of
662 thawing. Geophys. Res. Lett. 39, L15704, doi:10.1029/2012GL051958.

663 Hartley, I.P., Garnett, M.H., Sommerkorn, M., Hopkins, D.W., Fletcher, B.J., Sloan, V.L., Phoenix,
664 G.K., Wookey, P.A., 2012. A potential loss of carbon associated with greater plant growth in
665 the European Arctic. Nature Climate Change 2, 875–879.
666 Hayes, D.J., Kicklighter, D.W., McGuire, A.D., Chen, M., Zhuang, Q., Yuan, F., Melillo, J.M.,
667 Wullschleger, S.D., 2014. The impacts of recent permafrost thaw on land–atmosphere
668 greenhouse gas exchange. Environ. Res. Lett. 9, 045005.
669 Heimann, M. et al., 1998. Evaluation of terrestrial carbon cycle models through simulations of the
670 seasonal cycle of atmospheric CO2: First results of a model intercomparison study. Global
671 Biogeochem. Cycles 12 (1), 1–24.
672 Hobara, S., McCalley, C., Koba, K., Giblin, A.E., Weiss, M.S. Gettel, G.M., Shaver., G.R., 2006.
673 Nitrogen fixation in an arctic tundra watershed: a key atmospheric N source. Arctic, Antarctic,
674 and Alpine Research 38, 363-372.
675 Hugelius, G., Strauss, J., Zubrzycki, S., Harden, J.W., Schuur, E.A.G., Ping, C.-L.,
676 Schirrmeister, L., Grosse, G., Michaelson, G.J., Koven, C.D., O'Donnell, J.A., Elberling, B.,
677 Mishra, U., Camill, P., Yu, Z., Palmtag, J., Kuhry, P., 2014. Estimated stocks of circumpolar
678 permafrost carbon with quantified uncertainty ranges and identified data gaps. Biogeosciences
679 11, 6573-6593, doi:10.5194/bg-11-6573-2014.
680 Hugelius, G., Kuhry, P., Tarnocai, C., Virtanen, T., 2010. Soil Organic Carbon Pools in a
681 Periglacial Landscape; a Case Study from the Central Canadian Arctic. Permafrost Periglac. 21,
682 16-29.
683 IPCC, 2007. Climate Change 2007: The Physical Science Basis. Contribution of Working Group I
684 to the Fourth Assessment Report of the Intergovernmental Panel on Climate Change [S.

685 Solomon, D. Qin, M. Manning, Z. Chen, M. Marquis, K.B. Averyt, M.Tignor and H.L. Miller
686 (eds.)], Cambridge University Press, Cambridge, United Kingdom and New York, NY, USA.
687 Ise, T., Dunn, A.L., Wofsy, S.C., Moorcroft, P.R., 2008. High sensitivity of peat decomposition to
688 climate change through water-table feedback. Nature Geoscience 1(11), 763-766, doi:
689 10.1038/ngeo331.
690 Jiang, Y., Zhuang, Q., O'Donnell, J.A., 2012a. Modeling thermal dynamics of active layer soils
691 and near-surface permafrost using a fully coupled water and heat transport model. J. Geophys.
692 Res. 117, D11110, doi:10.1029/2012JD017512.
693 Jiang, Y., Zhuang, Q., Schaphoff, S., Sitch, S., Sokolov, A., Kicklighter, D., Melillo, J., 2012b.
694 Uncertainty analysis of vegetation distribution in the northern high latitudes during the 21st
695 century with a dynamic vegetation model. Ecology and Evolution. doi: 10.1002/ece3.85.
696 Jiang, Y., Rocha, A.V., O'Donnell, J.A., Drysdale, J.A., Rastetter, E.B., Shaver, G.R., Zhuang, Q.,
697 2015. Contrasting soil thermal responses to fire in Alaskan tundra and boreal forest. J. Geophys.
698 Res. Earth Surf. 120, 363-378.
699 Jobbagy, E. G., Jackson, R. B., 2000. The Vertical Distribution of Soil Organic Carbon and Its
700 Relation to Climate and Vegetation. Ecol. Appl. 10, 423-436.
701 Johnston, C.E., Ewing, S.A., Harden, J.W., Varner, R.K., Wickland, K.P., Koch, J.C., Fuller, C.C.,
702 Manies, K., Jorgenson, M.T., 2014. Effect of permafrost thaw on $CO_2$ and $CH_4$ exchange in a
703 western Alaska peatland chronosequence. Environ. Res. Lett. 9, 085004.
704 Jorgenson, M.T., Shur, Y.L., Pullman, E.R., 2006. Abrupt increase in permafrost degradation in
705 Arctic Alaska. Geophysical Research Letters 33, L02503, doi: 10D1029/2005GL024960.
706 Jorgenson, M.T., Racine, C.H., Walters, J.C., Osterkamp, T.E., 2001. Permafrost degradation and

ecological changes associated with a warming climate in central Alaska. Climatic Change 48(4), 551-571.

Kaminski, T., Heimann, M., Giering, R., 1999. A coarse grid three-dimensional global inverse model of the atmospheric transport: 2. Inversion of the transport of $CO_2$ in the 1980s. J. Geophys. Res. 105, 18555–18581.

Kanevskiy, M., Shur, Y., Fortier, D., Jorgenson, M.T., Stephani, E., 2011. Cryostratigraphy of late Pleistocene syngenetic permafrost (Yedoma) in northern Alaska, Itkillik River exposure. Quat. Res. 75(3), 584–596.

Keeling, C., Whorf, T., 2005. Atmospheric $CO_2$ records from sites in the SIO air sampling network. Trends: A Compendium of Data on Global Change. Carbon Dioxide Information Analysis Center, Oak Ridge National Laboratory, US Department of Energy, Oak Ridge, TN, USA.

Keuper, F., van Bodegom, P.M., Dorrepaal, E., Weedon, J.T., van Hal, J., van Logtestijn, R.S.P., Aerts, R., 2012. A frozen feast: thawing permafrost increases plant-available nitrogen in subarctic peatlands. Global Change Biology 18, 1998–2007.

Koch, J.C., Runkel, R.L., Striegl, R., McKnight, D.M., 2013. Hydrologic controls on the transport and cycling of carbon and nitrogen in a boreal catchment underlain by continuous permafrost. J. Geophys. Res. Biogeosci. 118, 698–712.

Koch, J.C., Kikuchi, C.P., Wickland, K.P., Schuster, P., 2014. Runoff sources and flow paths in a partially burned, upland boreal catchment underlain by permafrost. Water Resour. Res. 50, 8141–8158.

Koven, C.D., Ringeval, B., Friedlingstein, P., Ciais, P., Cadule, P., Khvorostyanov, D., Krinner, G., Tarnocai, C., 2011. Permafrost carbon-climate feedbacks accelerate global warming. P. Natl.

729 Acad. Sci. 108, 14769–14774, doi:10.1073/pnas.1103910108.
730 Koven, C. D., 2013. Boreal carbon loss due to poleward shift in low-carbon ecosystems. Nature
731 Geoscience 6, 452–456.
732 Lawrence, D.M., Slater, A.G., Swenson, S.C., 2012. Simulation of present-day and future
733 permafrost and seasonally frozen ground conditions in CCSM4. J. Clim. 25, 2207–2225.
734 Lloyd, A.H., Yoshikawa, K., Fastie, C.L., Hinzman, L., Fraver, M., 2003. Effects of permafrost
735 degradation on woody vegetation at arctic treeline on the Seward Peninsula, Alaska.
736 Permafrost and Periglacial Processes 14, 93–101.
737 MacDougall, A.H., Avis, C.A., Weaver, A.J., 2012. Significant contribution to climate warming
738 from the permafrost carbon feedback. Nature Geoscience doi:10.1038/ngeo1573.
739 Mack, M.C., Schuur, E.A.G., Bret-Harte, M.S., Shaver, G.R., Chapin, F.S., 2004. Ecosystem
740 carbon storage in arctic tundra reduced by long-term nutrient fertilization. Nature 431,
741 440–443.
742 McGuire, A.D., Christensen, T.R., Hayes, D. et al., 2012. An assessment of the carbon balance of
743 arctic tundra: comparisons among observations, process models, and atmospheric
744 inversions. Biogeosciences 9, 3185–3204.
745 Mitchell, T., Jones, P., 2005. An improved method of constructing a database of monthly climate
746 observations and associated high-resolution grids. Int. J. Climatol. 25, 693–712.
747 Nordin, A., Schmidt, I.K., Shaver, G.R., 2004. Nitrogen uptake by arctic soil microbes and plants
748 in relation to soil nitrogen supply. Ecology 85, 955-962.
749 O'Donnell, J.A., Harden, J.W., McGuire, A.D., Kanevskiy, M.Z., Jorgenson, M.T., Xu, X., 2011.
750 The effect of fire and permafrost interactions on soil carbon accumulation in an upland black

751 spruce ecosystem of interior Alaska: implications for post-thaw carbon loss. Global Change
752 Biology 17, 1461–1474.
753 Oechel, W.C., Vourlitis, G.L., Hastings, S.J., Ault, R.P., Bryant, P., 1998. The effects of water table
754 manipulation and elevated temperature on the net $CO_2$ flux of wet sedge tundra ecosystems.
755 Global Change Biology 4, 77–90.
756 Olefeldt, D., Roulet, N. T., Bergeron, O., Crill, P., Bäckstrand, K., Christensen, T. R., 2012. Net
757 carbon accumulation of a high-latitude permafrost palsa mire similar to permafrost-free
758 peatlands. Geophys. Res. Lett. 39, L03501, doi:10.1029/2011GL050355.
759 Olivas, P.C., Oberbauer, S.F., Tweedie, C.E., Oechel, W.C., Kuchy, A., 2010. Responses of $CO_2$
760 flux components of Alaskan Coastal Plain tundra to shifts in water table. J. Geophys. Res. 115,
761 G00I05, doi:10.1029/2009JG001254.
762 Osterkamp, T.E., 2007. Characteristics of the recent warming of permafrost in Alaska. Journal of
763 Geophysical Research-Earth Surface 112, F02S02, doi:10D1029/2006JF000578.
764 Osterkamp, T.E., Vierek, L., Shur, Y., Jorgenson, M.T., Racine, C., Doyle, A. Boone, R.D., 2000.
765 Observations of thermokarst and its impact on boreal forests in Alaska, U.S.A. Arctic,
766 Antarctic and Alpine Research 32, 303-315.
767 Rocha, A.V., Loranty, M.M., Higuera, P.E., Mack, M.C., Hu, F.S., Jones, B.M., Breen, A.L.,
768 Rastetter, E.B., Goetz, S.J., Shaver, G.R., 2012. The footprint of Alaskan tundra fires during
769 the past half-century: implications for surface properties and radiative forcing. Environ. Res.
770 Lett. 7, 044039.
771 Romanovsky, V.E., Osterkamp, T.E., 2000. Effects of unfrozen water on heat and mass transport
772 processes in the active layer and permafrost. Permafrost Periglac. 11, 219–239.

773 Romanovsky, V.E., Smith, S.L., Christiansen, H.H., Shiklomanov, N.I., Streletskiy, D.A., Drozdov,
774 D.S., Malkova, G.V., Oberman, N.G., Kholodov, A.L., Marchenko, S.S.. 2015. Terrestrial
775 Permafrost [in "State of the Climate in 2014"]. Bull. Amer. Meteor. Soc., 96 (7), S139-S141.
776 Saito, H., Šimůnek, J., Mohanty, B.P., 2006. Numerical analysis of coupled water, vapor, and heat
777 transport in the vadose zone, Vadose Zone J. 5, 784–800.
778 Scenarios Network for Alaska and Arctic planning, 2011. University of Alaska,
779 http://www.snap.uaf.edu.
780 Schaphoff, S., Heyder, U., Ostberg, S., Gerten, D., Heinke, J., Lucht, W., 2013. Contribution of
781 permafrost soils to the global carbon budget. Environmental Research Letters 8, 014026.
782 Schneider von Deimling, T., Meinshausen, M., Levermann, A., Huber, V., Frieler, K., Lawrence,
783 D.M., Brovkin, V., 2012. Estimating the near-surface permafrost-carbon feedback on global
784 warming. Biogeosciences, 9, 649–665, doi:10.5194/bg-9-649-2012.
785 Schuur, E.A.G., Abbott, B.W., Bowden, W.B. et al., 2013. Expert assessment of vulnerability of
786 permafrost carbon to climate change. Climatic Change 119, 359–374.
787 Schuur, E.A.G., Crummer, K.G., Vogel, J.G, Mack, M.C., 2007. Plant species composition and
788 productivity following permafrost thaw and thermokarst in Alaskan tundra. Ecosystems 10,
789 208–292.
790 Schuur, E.A.G., Vogel, J.G., Crummer, K.G., Lee, H., Sickman, J.O., Osterkamp, T.E., 2009. The
791 effect of permafrost thaw on old carbon release and net carbon exchange from tundra. Nature
792 459, 556–559.
793 Shaver, G.R., Bret-Harte, S.M., Jones, M.H., Johnstone, J., Gough, L., Laundre, J., Chapin, F.S.,
794 2001. Species composition interacts with fertilizer to control long-term change in tundra

795 productivity. Ecology 82, 3163–81.
796 Shur Y., French H.M., Bray M., Anderson D., 2004. Syngenetic permafrost growth:
797 cryostratigraphic observations from the CRREL Tunnel, Fairbanks, Alaska. Permafrost and
798 Periglacial Processes 15, 339–347.
799 Sitch, S., Smith, B., Prentice, I.C., Arneth, A., Bondeau, A., Cramer, W., Kaplan, J.O., Levis, S.,
800 Lucht, W., Sykes, M.T., Thonicke, K., Venevsky, S., 2003. Evaluation of ecosystem dynamics,
801 plant geography and terrestrial carbon cycling in the LPJ dynamic global vegetation model.
802 Glob. Change Biol. 9, 161–185.
803 Sitch, S. et al., 2008. Evaluation of the terrestrial carbon cycle, future plant geography and
804 climate-carbon cycle feedbacks using five Dynamic Global Vegetation Models (DGVMs).
805 Global Change Biol. 14, 2015 – 2039.
806 Slater, A.G., Lawrence, D.M., 2013. Diagnosing present and future permafrost from climate
807 models. Journal of Climate, 26(15), 5608-5623.
808 Smith, B., Warlind, D., Arneth, A., Hickler, T., Leadley, P., Siltberg, J. and Zaehle, S., 2014.
809 Implications of incorporating N cycling and N limitations on primary production in an
810 individual-based dynamic vegetation model. Biogeosciences, 11, 2027-2054.
811 Sokolov, A.P., Schlosser, C.A., Dutkiewicz, S., Paltsev, S., Kicklighter, D.W., Jacoby, H.D., Prinn,
812 R.G., Forest, C.E., Reilly, J., Wang, C., Felzer, B., Sarofim, M.C., Scott, J., Stone, P.H., Melillo,
813 J.M., Cohen, J., 2005. The MIT Integrated Global System Model (IGSM) Version 2: Model
814 Description and Baseline Evaluation. MIT Joint Program on the Science and Policy of Global
815 Change, Report 124, Cambridge, Massachusetts.
816 Sokolov, A.P., Kicklighter, D.W., Melillo, J.M., Felzer, B.S., Schlosser, C.A., Cronin, T.W., 2008.

817 Consequences of considering carbon-nitrogen interactions on the feedbacks between climate
818 and the terrestrial carbon cycle. Journal of Climate 21, 3776-3796.
819 Sokolov, A.P., Stone, P.H., Forest, C.E., Prinn, R.G., Sarofim, M.C., Webster, M., Paltsev, S.,
820 Schlosser, C.A., Kicklighter, D.W., Dutkiewicz, S., Reilly, J., Wang, C., Felzer, B., Jacoby, H.
821 D., 2009. Probabilistic forecast for 21st century climate based on uncertainties in emissions
822 (without policy) and climate parameters. Journal of Climate 22(19), 5175-5204.
823 Streletskiy, D.A., Sherstiukov, A.B., Frauenfeld, O.W. Nelson, F.E., 2015. Changes in the
824 1963–2013 shallow ground thermal regime in Russian permafrost regions. Environmental
825 Research Letters, 10(12), p.125005.
826 Sulman, B.N., Desai, A.R., Cook, B.D., Saliendra, N.Z., Mackay, D.S., 2009. Contrasting carbon
827 dioxide fluxes between a drying shrub wetland in Northern Wisconsin, USA, and nearby
828 forests. Biogeosciences 6, 1115-1126.
829 Sulman, B.N., Desai, A.R., Saliendra, N.Z., Lafleur, P.M., Flanagan, L.B., Sonnentag, O., Mackay,
830 D.S., Barr, A.G., van der Kamp, G., 2010. $CO_2$ fluxes at northern fens and bogs have opposite
831 responses to inter-annual fluctuations in water table. Geophysical Research Letters 37(19),
832 L19702, doi: 10.1029/2010GL044018.
833 Tarnocai, C., Canadell, J.G., Schuur, E.A.G., Kuhry, P., Mazhitova, G., Zimov, S., 2009. Soil
834 organic carbon pools in the northern circumpolar permafrost region. Global biogeochemical
835 cycles, 23(2).
836 Todd-Brown, K.E.O., Randerson, J.T., Post, W.M., Hoffman, F.M., Tarnocai, C., Schuur, E.A.G.,
837 Allison, S.D., 2013. Causes of variation in soil carbon simulations from CMIP5 Earth system
838 models and comparison with observations. Biogeosciences 10, 1717-1736.

839 Treat, C.C., Jones, M.C., Camill, P., Gallego-Sala, A., Garneau, M., Harden, J.W., Hugelius, G.,
840 Klein, E.S., Kokfelt, U., Kuhry, P. et al., 2016. Effects of permafrost aggradation on peat
841 properties as determined from a pan-Arctic synthesis of plant macrofossils. J. Geophys. Res.
842 Biogeosci. 121, 78–94.
843 Turetsky, M.R. et al., 2010. Recent acceleration of biomass burning and carbon losses in Alaskan
844 forests and peatlands. Nat. Geosci. 4, 27–31.
845 Walter-Anthony, K.M., Zimov, S.A., Grosse, G., Jones, M.C., Anthony, P.M., Chapin, F.S., Finlay,
846 J.C., Mack, M.C., Davydov, S., Frenzel, P., Frolking, S., 2014. A shift of thermokarst lakes
847 from carbon sources to sinks during the Holocene epoch. Nature 511, 452–456.
848 Wania, R., Ross, I., Prentice, I.C., 2009a. Integrating peatlands and permafrost into a dynamic
849 global vegetation model: 2. Evaluation and sensitivity of vegetation and carbon cycle processes.
850 Global Biogeochem. Cycles 23, GB3015, doi:10.1029/2008GB003413.
851 Wania, R., Ross, I., Prentice, I.C., 2009b. Integrating peatlands and permafrost into a dynamic
852 global vegetation model: 1. Evaluation and sensitivity of physical land surface processes.
853 Global Biogeochem. Cycles 23, GB3014, doi:10.1029/2008GB003412.
854 Webster, M., Sokolov, A.P., Reilly, J., Forest, C.E., Paltsev, S., Schlosser, C.A., Wang, C.,
855 Kicklighter, D.W., Sarofim, M., Melillo, J.M., Prinn, R.G., Jacoby, H.D., 2012. Analysis of
856 Climate Policy Targets under Uncertainty. Climatic Change 112, 569-583.
857 Xu, R., Prentice, I.C., 2008. Terrestrial nitrogen cycle simulation with a dynamic global vegetation
858 model. Global Change Biol. 14, 1745–1764.
859 Yoshikawa, K., Hinzman, L.D., 2003. Shrinking thermokarst ponds and groundwater dynamics in
860 discontinuous permafrost near Council, Alaska. Permafrost and Periglacial Processes 14(2),

151-160.

Yu, Z.C., Loisel, J., Brosseau, D.P., Beilman, D.W. Hunt, S.J. (2010) Global peatland dynamics since the last glacial maximum. Geophysical Research Letters 37, L13402, doi:10.1029/2010GL043584.

Zhang, Y., Chen, W.J., Riseborough, D.W., 2008. Transient projections of permafrost distribution in Canada during the 21st century under scenarios of climate change. Global and Planetary Change 60(3–4), 443–456.

Zobler, L., 1986. A world soil file for global climate modeling. National Aeronautics and Space Administration, Goddard Space Flight Center, Institute for Space Studies, NASA Technical Memorandum 87802, 32 pp.

871 **Table 1.** Changes in annual mean air temperature (ΔTair), annual total precipitation
872 (ΔPPT), and atmospheric $CO_2$ concentration ($\Delta CO_2$) between 2090s (2091-2100) and
873 2000s (2001-2010) in the six MIT IGSM climate scenarios used in this study (see
874 text). All differences are calculated over the region ranging from 45°N to 90°N.

| Scenario | ΔTair (°C) | ΔPPT (mm) | $\Delta CO_2$ (ppmv) |
|---|---|---|---|
| POL_L | 1.23 | 28.0 | 106 |
| POL_M | 1.70 | 40.5 | 93 |
| POL_H | 2.43 | 54.5 | 89 |
| REF_L | 5.01 | 94.5 | 530 |
| REF_M | 6.40 | 126.2 | 496 |
| REF_H | 8.42 | 162.4 | 488 |

875

876

877 **Table 2** Normalized Mean Squared Deviation (NMSD) between simulated and
878 observed seasonal cycle of $CO_2$; for comparison of the observed with the TM2
879 simulated seasonal cycles of $CO_2$, produced by coupling the monthly net ecosystem
880 productivity by LPJ and LPJ-STM for northern, tropical and southern monitoring
881 stations. The station data is from Heimann et al. (1998), for the period of 1983-1992.

| Station | Coordinate | LPJ | LPJ-STM | Average* |
|---|---|---|---|---|
| Alert, Northwest Territories | 82°27'N, 62°31'W | 17.8 | 14.3 | 28.4 |
| Point Barrow, Alaska | 71°19'N, 156°36'W | 12.3 | 11.5 | 13.2 |
| Cold Bay, Alaska | 55°12'N, 162°43'W | 10.5 | 5.8 | 11.1 |
| Cape Meares, Oregon | 45°29'N, 124°00'W | 6.7 | 4.3 | 18.6 |
| Azores (Terceira Island) | 38°45'N, 27°05'W | 1.7 | 1.1 | 4.0 |
| Niwot Ridge, Colorado | 40°03'N, 105°38'W | 6.1 | 3.0 | 5.9 |
| Sand Island, Midway | 28°13'N, 177°22'W | 9.4 | 4.5 | 8.8 |
| Key Biscayne, Florida | 24°40'N, 80°12'W | 6.4 | 3.7 | 9.7 |
| Cape Kumukahi, Hawaii | 19°31'N, 154°49'W | 29.4 | 16.8 | 14.7 |
| St. Croix, Virgin Islands | 17°45'N, 64°45'W | 9.2 | 6.3 | 6.2 |
| Seychelles (Mahe Island) | 4°40'S, 55°10'E | 2.2 | 1.9 | 1.0 |
| Ascension Island | 7°55'S, 14°25'W | 4.3 | 4.1 | 10.6 |
| American Samoa | 14°15'S, 170°34'W | 1.3 | 1.4 | 5.2 |
| Cape Grim, Tasmania | 40°41'S, 144°41'E | 1.6 | 1.1 | 17.4 |
| Amundsen Scott (South Pole) | 89°59'S, 24°48'W | 6.5 | 5.8 | 34.7 |

882 *The mean value of NMSDs from five prognostic models (BIOME2, FBM, SILVAN, and TEM)

used in Heimann et al. (1998).

$$NMSD = \frac{1}{12}\sum_{m=1}^{12}\left(\frac{C_{T,m} + C_{F,m} + C_{O,m} - C_{OBS,m}}{\sigma_m}\right)^2$$ NMSD is calculated as the normalized square of difference between the sum of monthly $CO_2$ concentration from biospheric ($C_{T,m}$), fossil fuel ($C_{F,m}$), ocean flux ($C_{O,m}$), and the 10-year mean of observed $CO_2$ flux values ($C_{OBS,m}$) for the period 1983-1992. The factor used to normalized the difference is the standard deviation ($\sigma_m$) of the observed value for each month (m = 1,…,12) of the year.

890 **Table 3** The average carbon stocks in the 1900s, 2010s and 2090s estimated with LPJ and LPJ-STM.

| | **Vegetation carbon (Pg C)** | | | | | | **Soil carbon (Pg C)** | | | | | |
|---|---|---|---|---|---|---|---|---|---|---|---|---|
| | **LPJ** | | | **LPJ-STM** | | | **LPJ** | | | **LPJ-STM*** | | |
| | **1900s** | **2010s** | **2090s** | **1900s** | **2010s** | **2090s** | **1900s** | **2010s** | **2090s** | **1900s** | **2010s** | **2090s** |
| **Historical** | 165.0 | - | - | 178.7 | - | - | 867.1 | - | - | 1297.3 | - | - |
| **POL_L** | - | 210.7 | 336.4 | - | 228.8 | 358.0 | - | 864.1 | 837.6 | - | 1319.4 | 1350.8 |
| **POL_M** | - | 210.2 | 326.3 | - | 227.8 | 347.6 | - | 864.0 | 833.4 | - | 1319.3 | 1335.6 |
| **POL_H** | - | 211.7 | 334.1 | - | 228.9 | 355.7 | - | 864.0 | 825.4 | - | 1319.3 | 1322.1 |
| **REF_L** | - | 210.6 | 333.4 | - | 228.0 | 355.7 | - | 863.9 | 827.1 | - | 1319.5 | 1335.6 |
| **REF_M** | - | 210.1 | 316.3 | - | 227.7 | 337.3 | - | 864.1 | 818.6 | - | 1319.7 | 1314.4 |
| **REF_H** | - | 211.8 | 275.7 | - | 229.4 | 294.1 | - | 864.0 | 805.2 | - | 1319.3 | 1292.2 |

891 ***** Note that the top 3 m soil C stock in LPJ-STM were used to compare with the soil C pool modeled with LPJ, which does not explicitly model

892 soil carbon at different depths.

893 **Table 4** Mean annual carbon fluxes (Pg C $yr^{-1}$) for the 2000s and 2090s estimated with LPJ and LPJ-STM.

| | **LPJ** | | | | | | **LPJ-STM** | | | | | |
|---|---|---|---|---|---|---|---|---|---|---|---|---|
| | **NPP** | | **$R_H$** | | **NEP** | | **NPP** | | **$R_H$** | | **NEP** | |
| | **2000s** | **2090s** | **2000s** | **2090s** | **2000s** | **2090s** | **2000s** | **2090s** | **2000s** | **2090s** | **2000s** | **2090s** |
| **POL_L** | 16.7 | 18.3 | 14.9 | 16.3 | 1.8 | 2.0 | 17.2 | 18.8 | 14.4 | 16.3 | 2.8 | 2.5 |
| **POL_M** | 16.6 | 18.2 | 14.8 | 16.7 | 1.8 | 1.5 | 17.1 | 18.8 | 14.4 | 16.6 | 2.7 | 2.2 |
| **POL_H** | 16.8 | 18.8 | 14.9 | 17.3 | 1.9 | 1.5 | 17.4 | 19.4 | 14.5 | 17.4 | 2.9 | 2.0 |
| **REF_L** | 16.6 | 24.4 | 14.9 | 24.0 | 1.7 | 0.4 | 17.2 | 25.2 | 14.5 | 24.1 | 2.7 | 1.1 |
| **REF_M** | 16.6 | 25.1 | 14.7 | 26.0 | 1.9 | -0.9 | 17.1 | 25.9 | 14.4 | 26.2 | 2.7 | -0.3 |
| **REF_H** | 16.9 | 26.9 | 14.9 | 31.1 | 2.0 | -4.2 | 17.4 | 27.8 | 14.5 | 31.4 | 2.9 | -3.6 |

894

# Figure caption

**Fig. 1.** Diagram illustrating hydrologic modeling framework in relation to soil profile structure. Vertical soil structure is divided into seven distinct layers (3 organic horizons, 3 mineral horizons and a deep horizon) that vary with respect to hydraulic properties (k, porosity, etc.). The model tracks and quantifies different water fluxes including precipitation (Pr), interception by vegetation ($E_I$); snow melt water (M), evaporation ($E_s$) transpiration ($E_T$) runoff ($R_{surface}$),subsurface flow ($R_{subsurface}$), and percolation or infiltration ($R_{perc}$). The solid arrows (→) reflect infiltration pathways of precipitation and snowmelt, which can be transferred from the ground surface to any of the top four layers. The dashed arrows (- - >) reflect vertical water loss pathways via $E_s$ and $E_T$, which can originate from the top three organic horizons or the uppermost mineral horizon. The dashed-dotted arrows (– · –>) reflect downward migration of soil water (i.e. $R_{perc}$) which can occur across all soil horizons. The dotted arrows (· · ·>) indicate either pathways of $R_{surface}$ at the ground surface, or $R_{subsurface}$ from the B or C mineral horizons.

**Fig. 2.** LPJ-STM simulated (top) and observed (bottom) soil temperature profile at the Westdock site (using probe 2 data).

**Fig. 3.** Difference in soil moisture at 25 cm by LPJ and LPJ-STM relative to observations at three sites.

**Fig. 4.** Observed and simulated daily soil temperature at 25 cm with STM and the soil temperature algorithm in LPJ at eight sites. RMSE represents the root mean square error from the fit between observations and simulations. AT: Atqasuk (70.5$^{o}$, -157.5$^{o}$); BP: Betty Pingo (70.5$^{o}$, -149$^{o}$); TL: Toolik (68.5$^{o}$, -149.5$^{o}$); WD: Westdock (70.5$^{o}$, -148.5$^{o}$). BP-1 and BP-2 are two different sites, and WD-1, 2, 3, 4 are four different sites.

**Fig. 5.** Modeled distribution of active layer thickness (ALT) in areas underlain by permafrost in 2000 (left) and a comparison (right) between modeled and observed ALT at 172 sites derived from the GTN-P database (Biskaborn et al., 2015). The dash line represents the 1:1 line.

**Fig. 6.** Observed and simulated monthly NEP (g C m$^{-2}$, positive value means a C flux to the biosphere, and negative value represents a C flux to the atmosphere) with LPJ and LPJ-STM at nine sites (latitude and longitude shown in parentheses) located north of latitude 45$^{o}$N. $R^2$ represents the coefficient of determination from simple linear regressions. Observed NEP data were obtained via the FLUXNET database (http://fluxnet.ornl.gov).

**Fig. 7.** Time series of near surface permafrost extent in the 45$^{o}$N northward region simulated with LPJ-STM for the historical and projection periods. Near-surface permafrost extent is the integrated area of 0.5$^{o}$ × 0.5$^{o}$ grid cells with the maximum

939 active layer shallower than 3 m.

940

941 **Fig. 8.** Difference (LPJ-STM minus LPJ) in modeled annual net primary production
942 (NPP), heterotrophic respiration ($R_H$) and net ecosystem productivity (NEP) of the
943 circumpolar north for the historical period and six future projections.

944

945 **Fig. 9.** Distribution of the differences (LPJ-STM minus LPJ) of modeled mean annual
946 carbon fluxes (ΔNEP, ΔRH, ΔNEP) and mean carbon standing stocks (Δvegetation C,
947 Δsoil C, Δecosystem C stocks) during the 2000s for the circumpolar region north of
948 $45^{o}$N.

949

950 **Fig. 10.** Carbon density (kg C $m^{-2}$) in the top 30 cm (a) and 100 cm (b) of soil
951 estimated by LPJ-STM for the year 2000, the Northern Circumpolar Soil Carbon
952 Database version 2 (NCSCDv2, Hugelius et al., 2014), and the Harmonized World
953 Soil Database (HWSD, FAO/IIASA/ISRIC/ISSCAS/JRC, 2012).

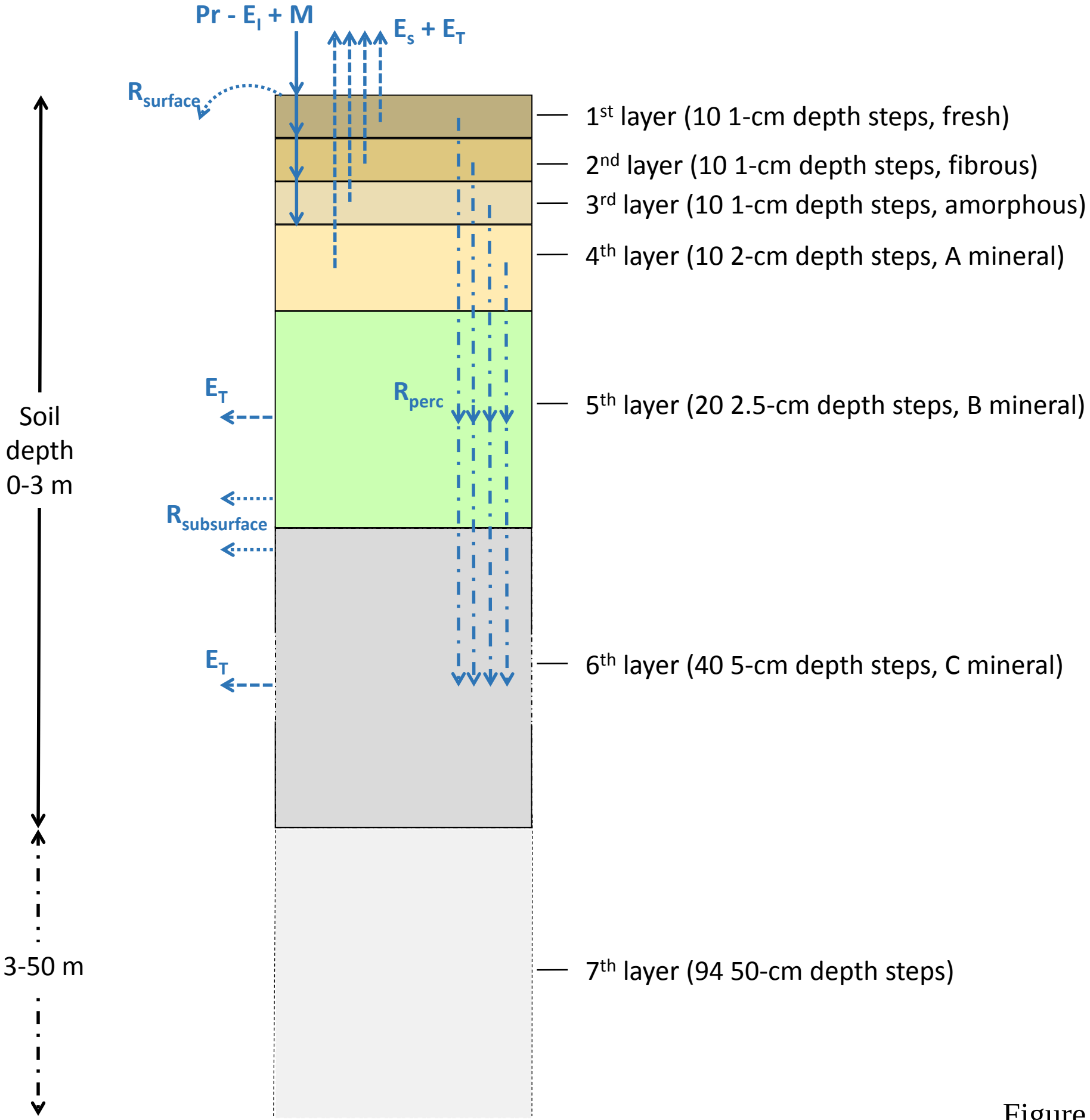
Pr - E_I + M
E_S + E_T
R_surface
1st layer (10 1-cm depth steps, fresh)
2nd layer (10 1-cm depth steps, fibrous)
3rd layer (10 1-cm depth steps, amorphous)
4th layer (10 2-cm depth steps, A mineral)
E_T
R_perc
5th layer (20 2.5-cm depth steps, B mineral)
R_subsurface
E_T
6th layer (40 5-cm depth steps, C mineral)
Soil depth 0-3 m
3-50 m
7th layer (94 50-cm depth steps)

Figure 1.

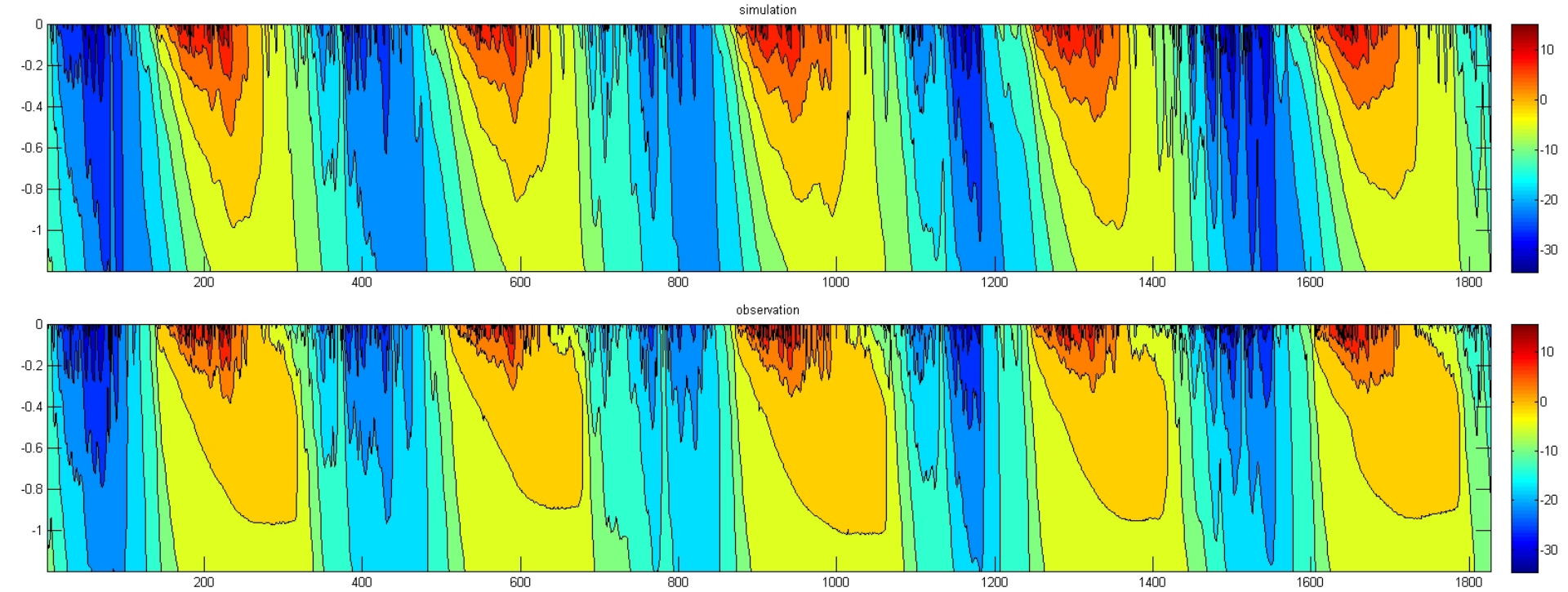
simulation
0
-0.2
-0.4
-0.6
-0.8
-1
200
400
600
800
1000
1200
1400
1600
1800
10
0
-10
-20
-30
observation
0
-0.2
-0.4
-0.6
-0.8
-1
200
400
600
800
1000
1200
1400
1600
1800
10
0
-10
-20
-30

Figure 2.

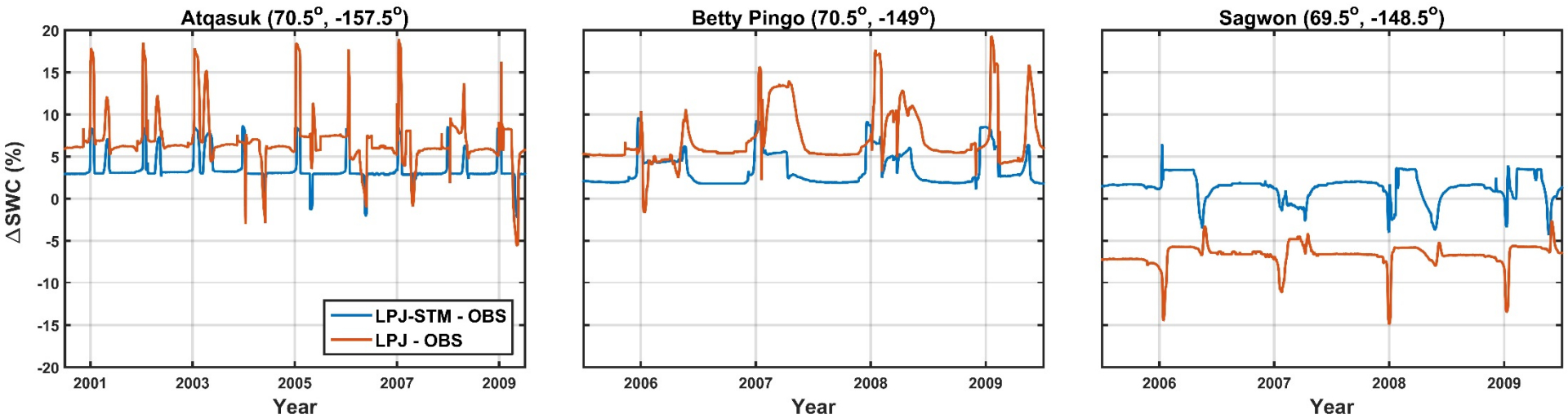
Atqasuk (70.5°, -157.5°)
Betty Pingo (70.5°, -149°)
Sagwon (69.5°, -148.5°)
ΔSWC (%)
Year
LPJ-STM - OBS
LPJ - OBS

Figure 3.

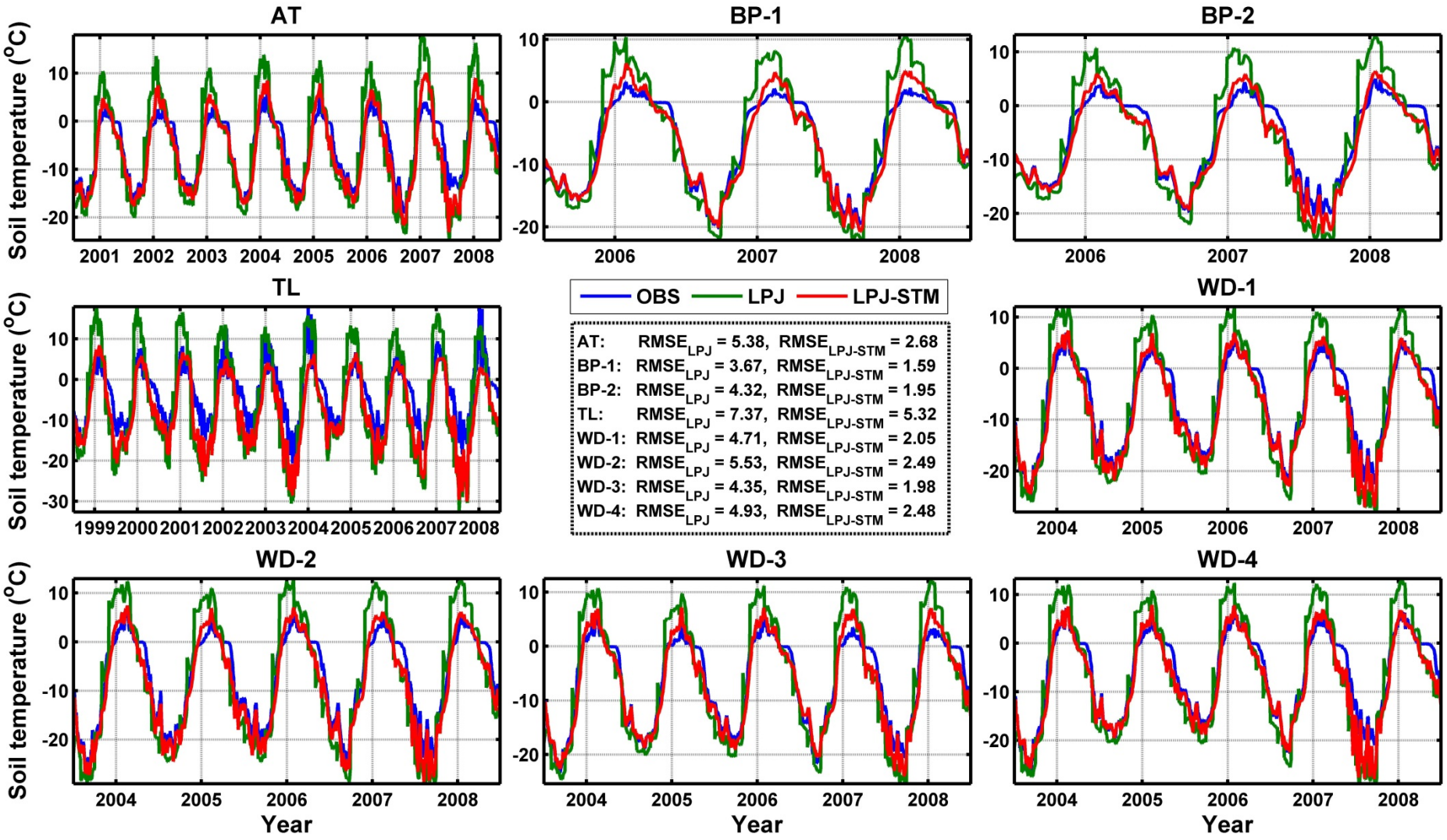
AT
BP-1
BP-2
TL
WD-1
WD-2
WD-3
WD-4
Soil temperature (°C)
Year
OBS
LPJ
LPJ-STM
AT: RMSE_LPJ = 5.38, RMSE_LPJ-STM = 2.68
BP-1: RMSE_LPJ = 3.67, RMSE_LPJ-STM = 1.59
BP-2: RMSE_LPJ = 4.32, RMSE_LPJ-STM = 1.95
TL: RMSE_LPJ = 7.37, RMSE_LPJ-STM = 5.32
WD-1: RMSE_LPJ = 4.71, RMSE_LPJ-STM = 2.05
WD-2: RMSE_LPJ = 5.53, RMSE_LPJ-STM = 2.49
WD-3: RMSE_LPJ = 4.35, RMSE_LPJ-STM = 1.98
WD-4: RMSE_LPJ = 4.93, RMSE_LPJ-STM = 2.48

Figure 4.

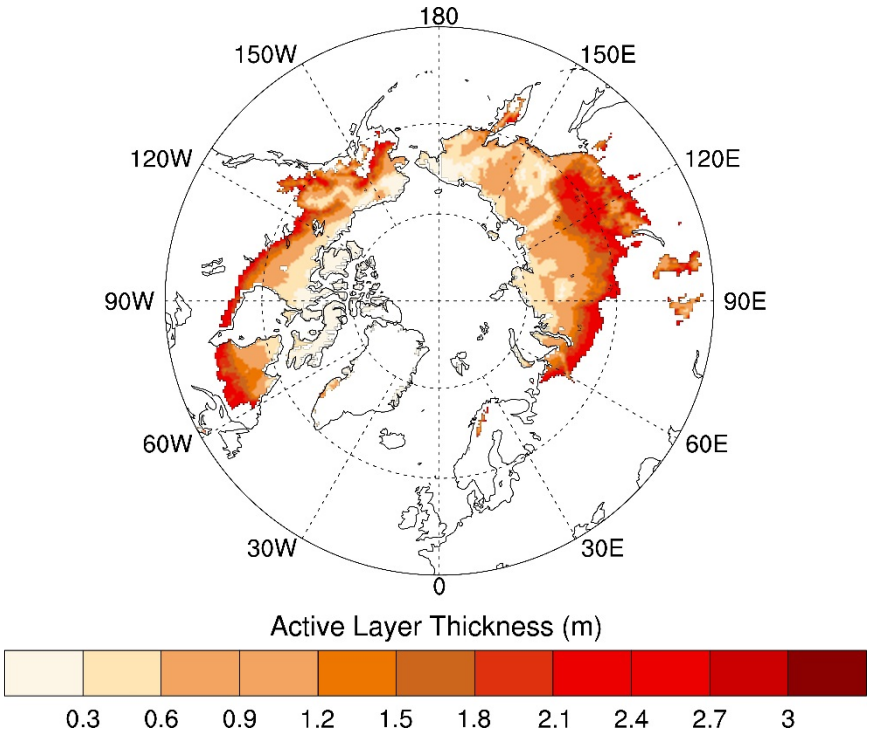
180
150W
150E
120W
120E
90W
90E
60W
60E
30W
30E
0
Active Layer Thickness (m)
0.3
0.6
0.9
1.2
1.5
1.8
2.1
2.4
2.7
3

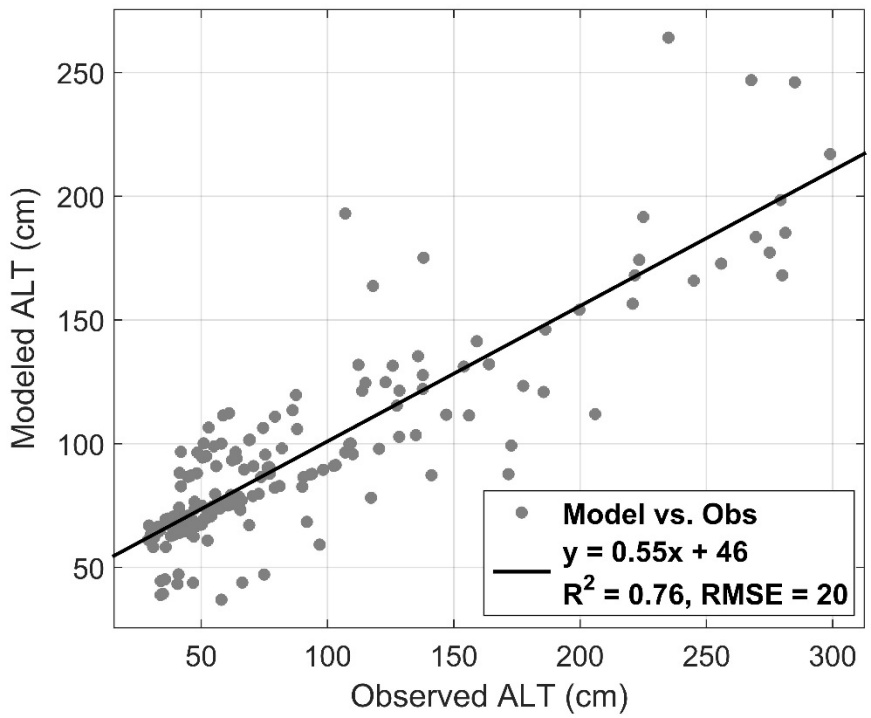
Modeled ALT (cm)
Observed ALT (cm)
50
100
150
200
250
300
Model vs. Obs
y = 0.55x + 46
R2 = 0.76, RMSE = 20

Figure 5.

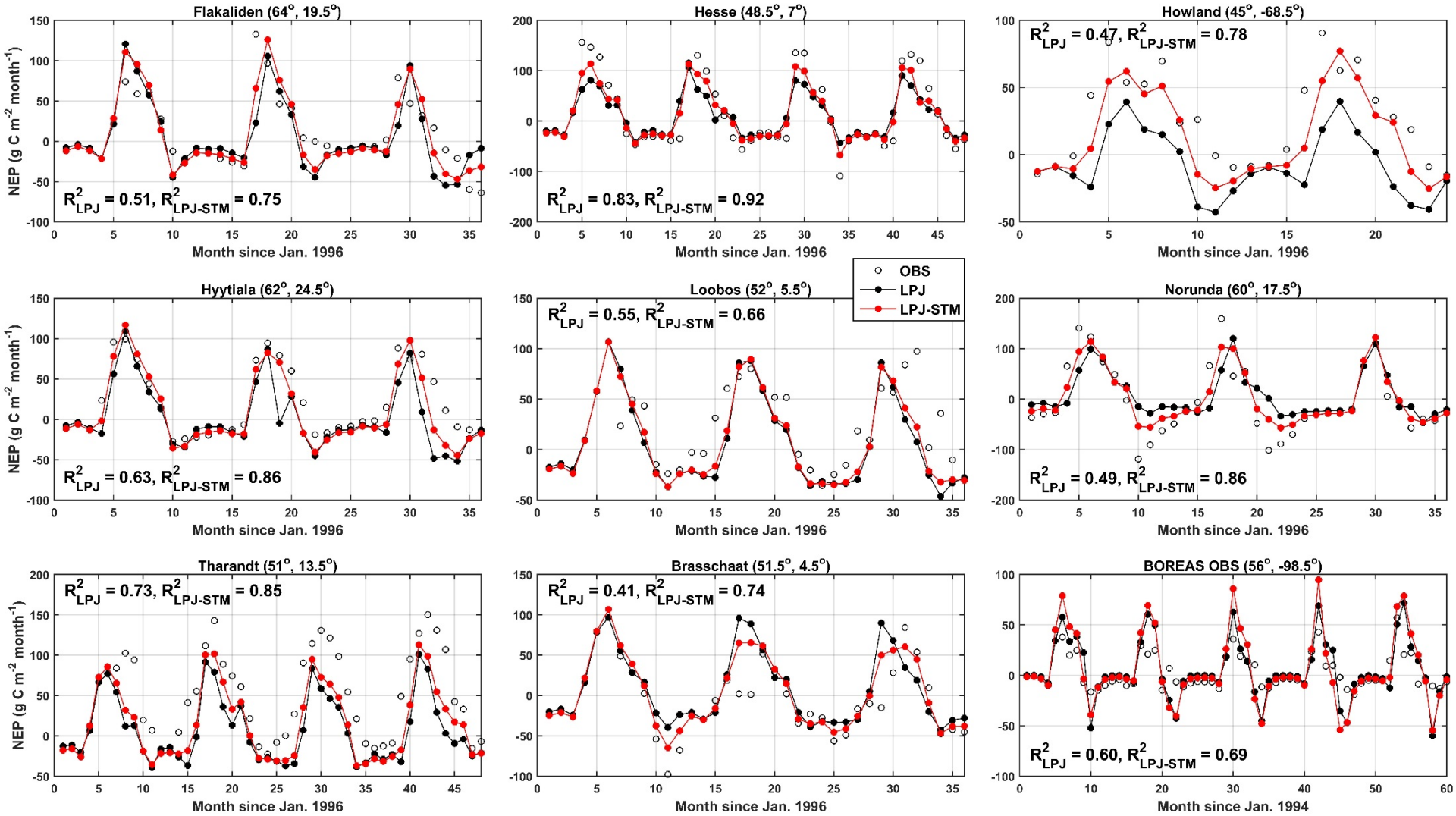
Flakaliden (64°, 19.5°)
Hesse (48.5°, 7°)
Howland (45°, -68.5°)
Hyytiala (62°, 24.5°)
Loobos (52°, 5.5°)
Norunda (60°, 17.5°)
Tharandt (51°, 13.5°)
Brasschaat (51.5°, 4.5°)
BOREAS OBS (56°, -98.5°)
OBS
LPJ
LPJ-STM
NEP (g C m-2 month-1)
Month since Jan. 1996
Month since Jan. 1994
R2LPJ = 0.51, R2LPJ-STM = 0.75
R2LPJ = 0.83, R2LPJ-STM = 0.92
R2LPJ = 0.47, R2LPJ-STM = 0.78
R2LPJ = 0.63, R2LPJ-STM = 0.86
R2LPJ = 0.55, R2LPJ-STM = 0.66
R2LPJ = 0.49, R2LPJ-STM = 0.86
R2LPJ = 0.73, R2LPJ-STM = 0.85
R2LPJ = 0.41, R2LPJ-STM = 0.74
R2LPJ = 0.60, R2LPJ-STM = 0.69

Figure 6.

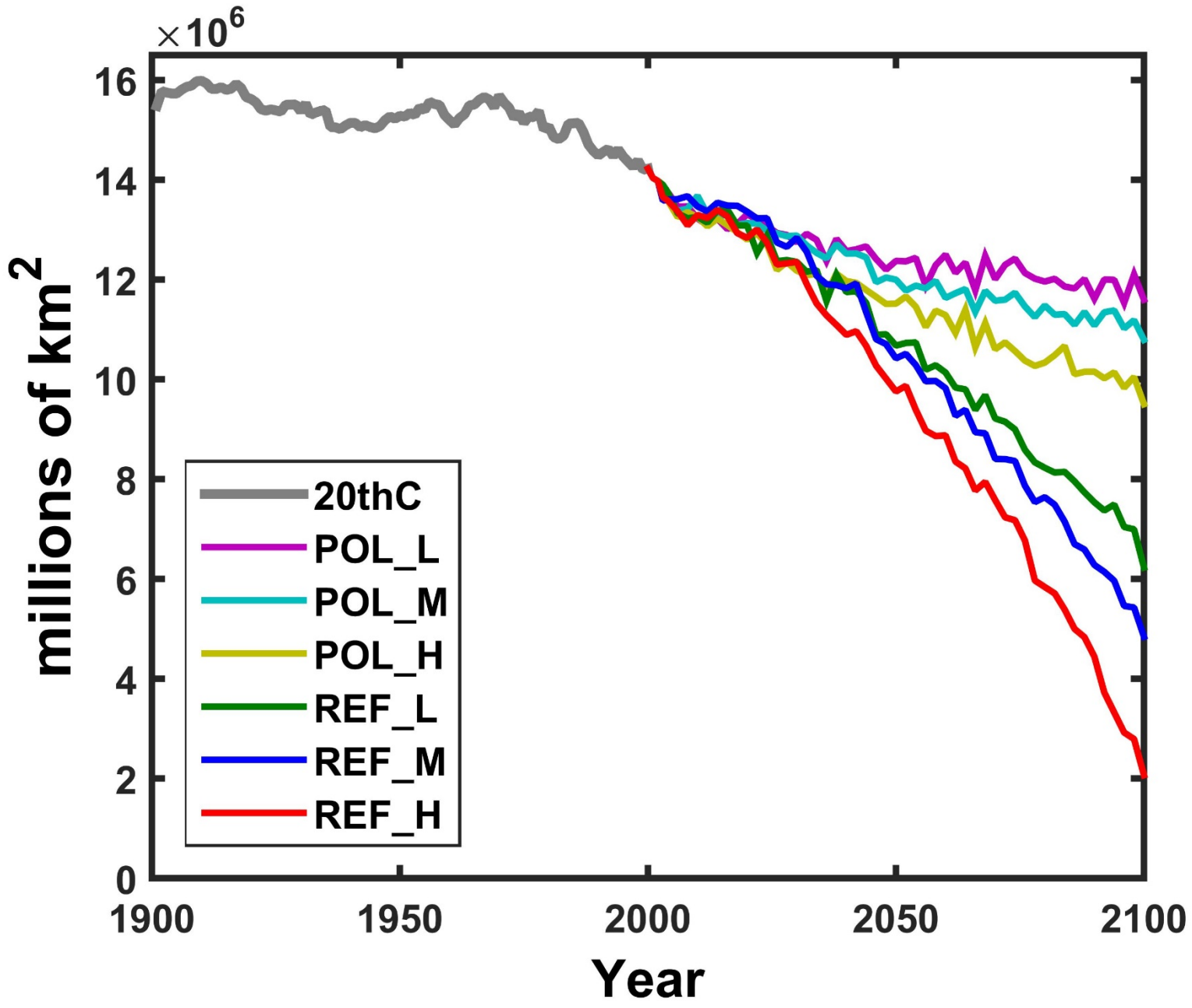
×10^6
16
14
12
10
8
6
4
2
0
millions of km^2
1900
1950
2000
2050
2100
Year
20thC
POL_L
POL_M
POL_H
REF_L
REF_M
REF_H

Figure 7.

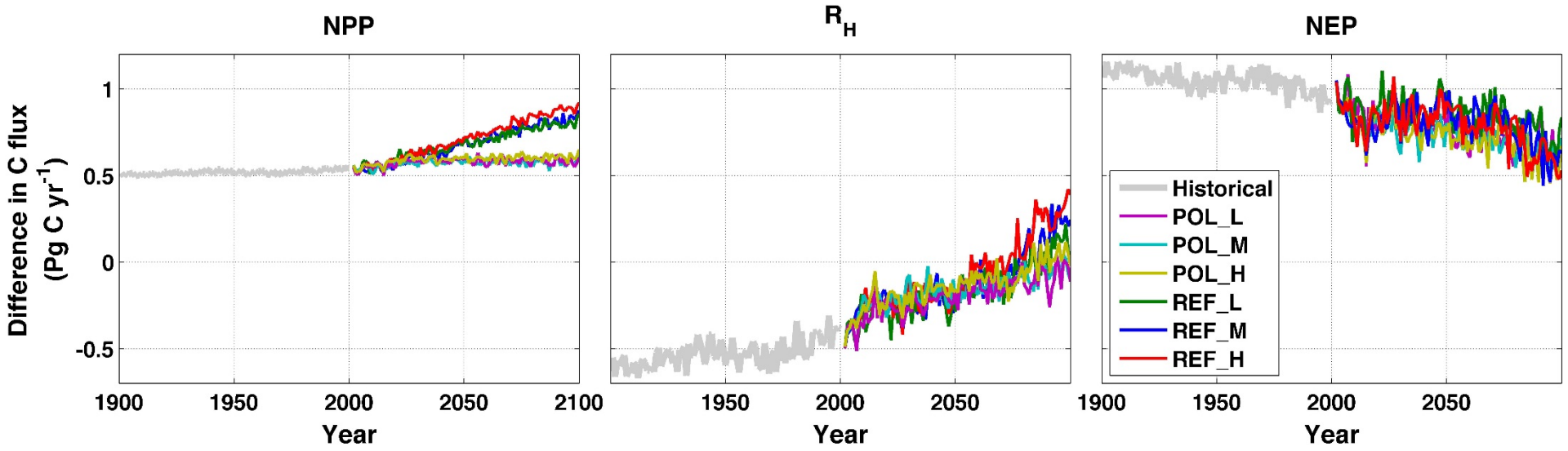
NPP
R_H
NEP
Difference in C flux
(Pg C yr^-1)
1
0.5
0
-0.5
1900
1950
2000
2050
2100
Year
Historical
POL_L
POL_M
POL_H
REF_L
REF_M
REF_H

Figure 8.

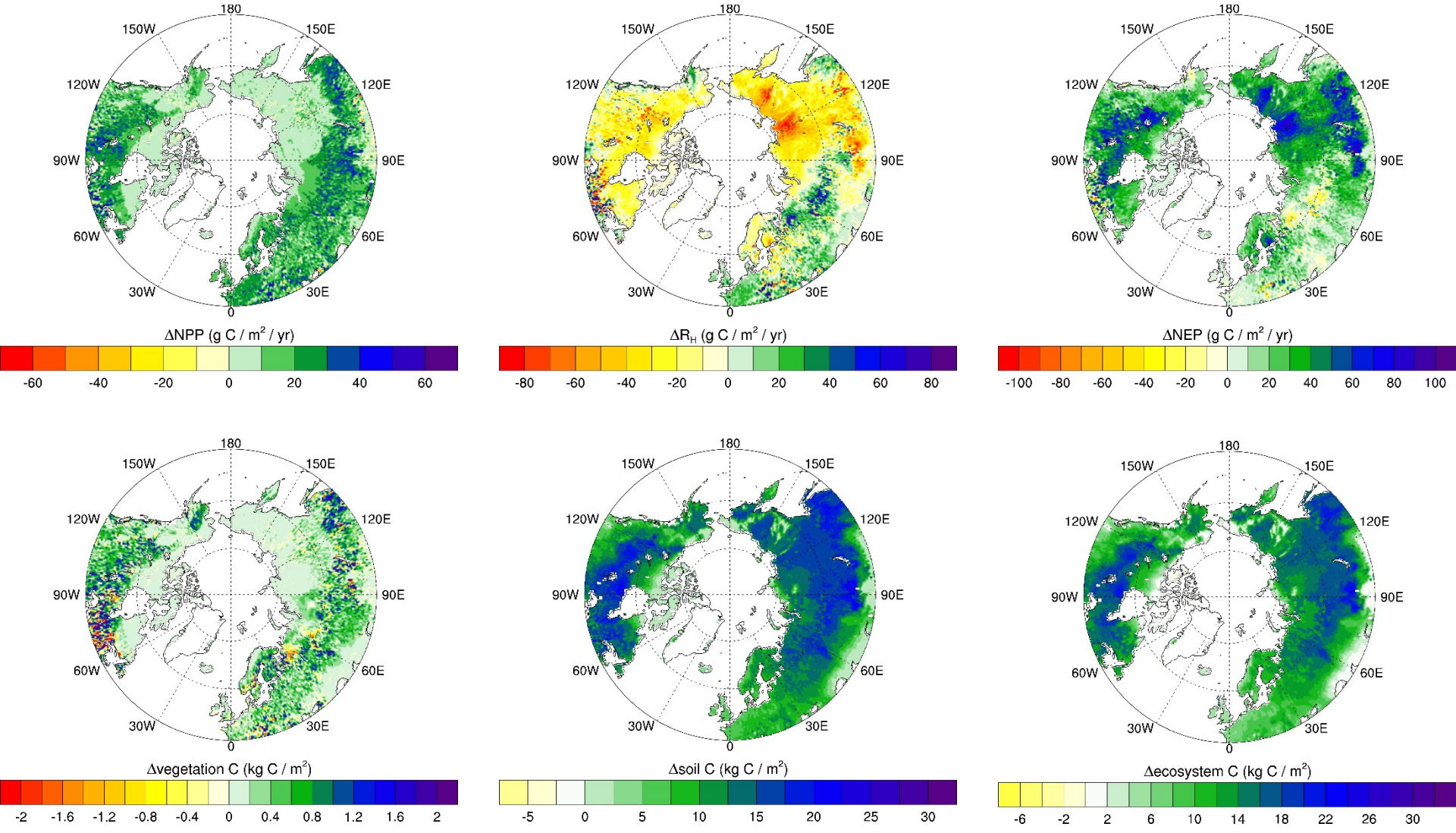
180
150W
150E
120W
120E
90W
90E
60W
60E
30W
30E
0
ΔNPP (g C / m² / yr)
-60 -40 -20 0 20 40 60
ΔR_H (g C / m² / yr)
-80 -60 -40 -20 0 20 40 60 80
ΔNEP (g C / m² / yr)
-100 -80 -60 -40 -20 0 20 40 60 80 100
Δvegetation C (kg C / m²)
-2 -1.6 -1.2 -0.8 -0.4 0 0.4 0.8 1.2 1.6 2
Δsoil C (kg C / m²)
-5 0 5 10 15 20 25 30
Δecosystem C (kg C / m²)
-6 -2 2 6 10 14 18 22 26 30

Figure 9.

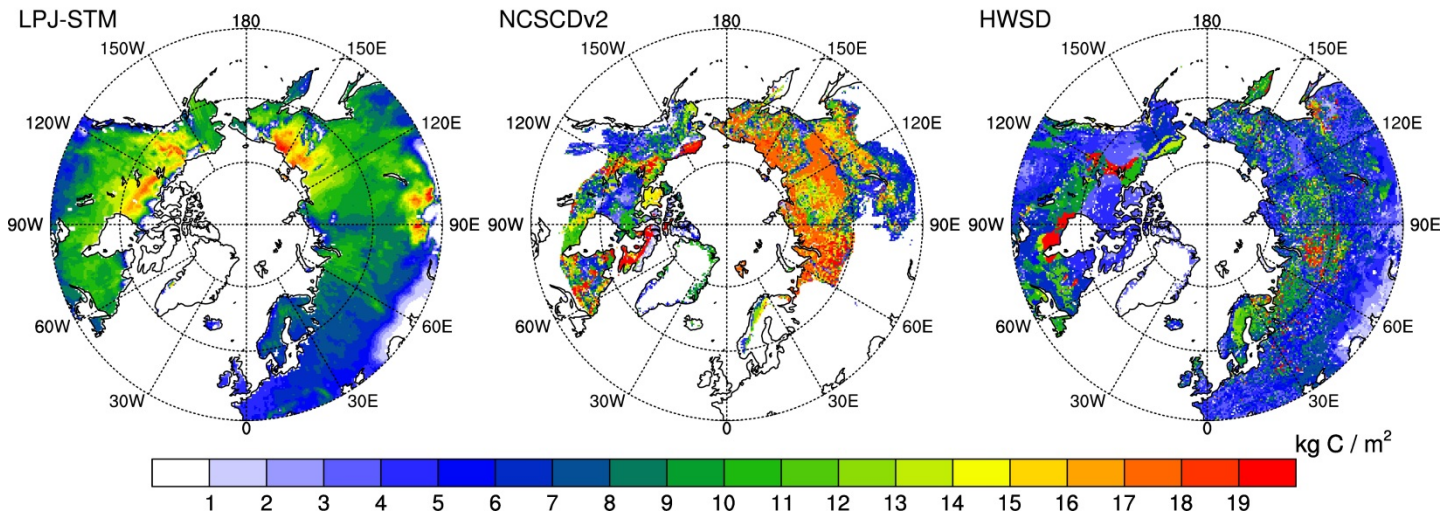
LPJ-STM
NCSCDv2
HWSD
180
150W
150E
120W
120E
90W
90E
60W
60E
30W
30E
0
kg C / m2
1
2
3
4
5
6
7
8
9
10
11
12
13
14
15
16
17
18
19

Figure 10. (a)

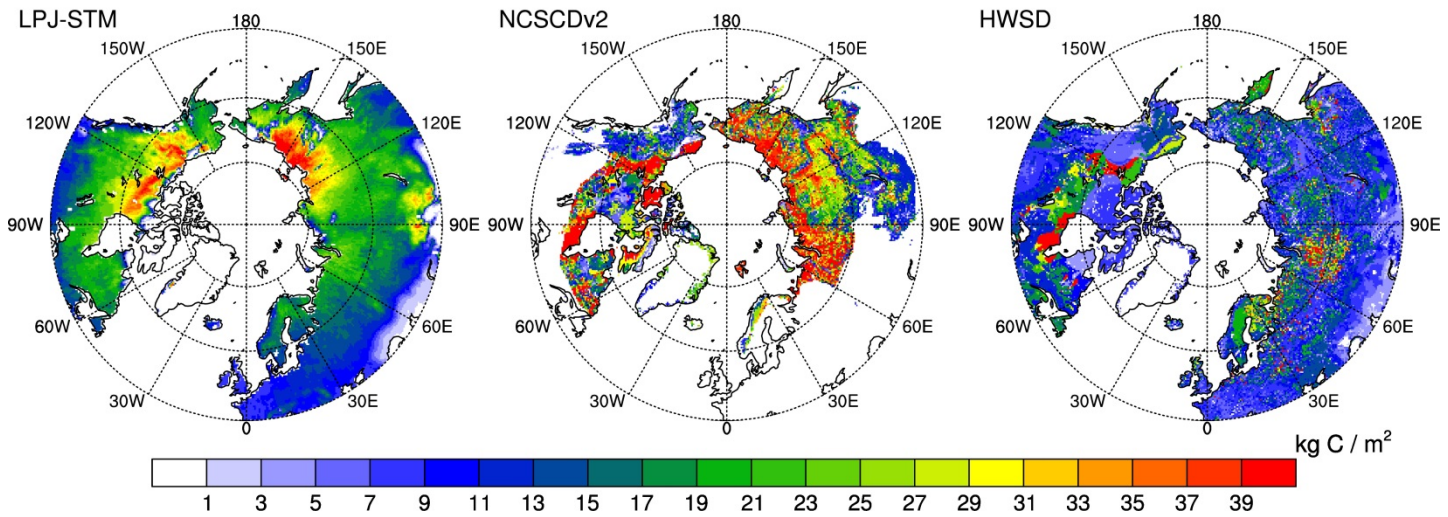
LPJ-STM
NCSCDv2
HWSD
180
150W
150E
120W
120E
90W
90E
60W
60E
30W
30E
0
kg C / m2
1 3 5 7 9 11 13 15 17 19 21 23 25 27 29 31 33 35 37 39

Figure 10. (b)